Available online at www.sciencedirect.com

ScienceDirect

Advances in Space Research 78 (2026) 9389–9408

ADVANCES IN SPACE RESEARCH
(a COSPAR publication)

www.elsevier.com/locate/asr

Analytical gravity field error analysis of multiple pair constellations

Gabriel Valles-Valverde [a,b,*], Ernst J.O. Schrama [b], João Teixeira da Encarnação [b]

[a] Institute of Geodesy, TU Graz, Steyrergasse 30, Graz 8010, Austria
[b] Delft University of Technology, Kluyverweg 1, Delft 2629 HS, Netherlands

Received 1 May 2026; received in revised form 9 July 2026; accepted 17 August 2026
Available online 22 August 2026

Abstract

The GRACE and GRACE-FO missions have provided monthly gravity field models for more than 20 years. The upcoming GRACE-C mission will guarantee data continuation for the next decade following the concept of a pair of satellites flying in a polar orbit for global coverage. Along with an additional satellite pair flying in an inclined orbit, the two satellite pairs will form a Bender constellation resulting in the MAGIC mission. As a result, both temporal and spatial resolution of Earth's gravity field will improve. The novel mission configuration, however, poses new challenges for mission design, such as optimal selection of the constellation orbital parameters. In this work, the lumped coefficients theory is employed to propagate the error spectra of inter-satellite range and GNSS observations to the Stokes coefficients representing the gravity field. Noise propagation from accelerometers and attitude noise to the observations is also considered. This methodology is computationally much more efficient than error analysis studies from full end-to-end simulation. Thus, the design space can be quickly explored to determine a global optimal inclination for the second pair, for example. However, the analytical methodology presents some limitations, mainly the stationarity of observation noise. Therefore, we do not consider background model errors and temporal aliasing cannot be accounted for. Nonetheless, it can be circumvented directly observing the high-frequency signals at daily and sub-daily timescales. Multiple pair constellations are a promising mission concept in this regard. This provides a framework for leveraging the benefits of the analytical methodology. We apply the lumped coefficients theory to multiple pair constellations and analyse their spatio-temporal resolution for constellations up to 100 satellite pairs.

Keywords: Satellite gravimetry; Error analysis; Lumped series; Multiple pair constellations

1. Introduction

The Earth's gravity field changes in time as undergoing geophysical processes cause mass redistributions within our planet. In this way, monitoring the gravity field provides valuable insights with endless applications in climate monitoring or Earth system sciences.

For more than two decades, the Gravity Recovery And Climate Experiment (GRACE) (Tapley et al., 2004) and GRACE Follow-On (GRACE-FO) (Landerer et al., 2020) missions have been monitoring the gravity field of the Earth. The missions implement the low-low concept of Satellite-to-Satellite Tracking (ll-SST) (Wolff, 1969), which avoids atmospheric errors from ground observations and allows for micrometer to nanometer inter-satellite distance measurements. The same concept is employed in the Gravity Recovery And Interior Laboratory (GRAIL) mission (Zuber et al., 2013) to measure the gravity field of the Moon with high resolution, reaching scales below 5 km (Goossens et al., 2020). The high-low (hl-SST) concept has been realized, for example, through GNSS observations as part of the Challenging Minisatellite Payload (CHAMP) mission (Reigber et al., 2002), or for the Swarm

* Corresponding author at: Institute of Geodesy, TU Graz, Steyrergasse 30, Graz 8010, Austria.

E-mail addresses: gabriel.vallesvalverde@tugraz.at (G. Valles-Valverde), e.j.o.schrama@tudelft.nl (E.J.O. Schrama), j.g.deteixeiradaencarnacao@tudelft.nl (J. Teixeira da Encarnação).

https://doi.org/10.1016/j.asr.2026.08.045
0273-1177/© 2026 The Author(s). Published by Elsevier B.V. on behalf of COSPAR.

satellites (da Encarnação et al., 2016). Alternatively, the Gravity field and steady-state Ocean Circulation Explorer (GOCE) mission (Drinkwater et al., 2007) measured the static gravity field of the Earth employing gravity gradiometry. Nonetheless, the gradiometer can be conceived as the same mission concept with much shorter baselines that fit inside a single satellite (Rummel and Colombo, 1985).

Despite their success, GRACE and GRACE-FO performance has limited temporal and spatial resolution for societal and scientific needs (Pail et al., 2015). For example, water mass redistribution associated with ocean and atmospheric tides occurs at high temporal frequencies, down to sub-daily timescales, far below current GRACE temporal resolution. Non-tidal processes such as pressure redistribution also contribute to gravity field changes at these higher temporal frequencies. Continental hydrology, among others, becomes relevant at smaller spatial scales. For instance, the spatial scale of the ground water storage signal ranges from a few 10 km to 1000 km, while other land hydrology signals such as soil moisture, surface water or snow water are relevant below a few 100 km. Currently, GRACE spatial resolution about 550 km in monthly timescales only covers about 10% of river basins worldwide, which compromises closure of terrestrial water balance (Famiglietti and Rodell, 2013). Many other limitations, also in other fields such as cryosphere or solid Earth sciences, are discussed by the International Union of Geodesy and Geophysics (IUGG) in Pail et al. (2015).

In the processing of gravity field solutions, the undersampled signals have to be properly reduced; otherwise, they alias into the solutions, degrading their quality. For this purpose, background models are employed, but they are imperfect and residual signals remain, contaminating the solutions (Han et al., 2004). This is one of the main limiting factors for the quality of the gravity field solutions derived from GRACE and GRACE-FO (Flechtner et al., 2015).

The gravity field errors are larger in lower latitudes because fewer samples per unit area are taken on this region due to the polar orbit. Furthermore, GRACE observations persistently sample in north–south direction. Therefore, there is little sensitivity to east–west direction, especially around the equator. To improve the isotropy of the observations, Bender et al. (2008) proposed an additional pair of satellites at a lower inclination. The Bender configuration has been selected as part of the ESA/NASA joint MAGIC (MAss Change and Geosciences International Constellation) mission (Haagmans et al., 2020) with the aim to improve the spatio-temporal resolution of Earth's gravity field. The polar pair (P1) consists of the joint NASA/DLR GRACE-Continuity (GRACE-C) mission, while the inclined pair (P2) is developed by ESA as part of the Next Generation Gravity Mission (NGGM) (Daras et al., 2023a; Massotti et al., 2023). MAGIC will employ orbits with fast repeating ground-tracks to attain weekly or sub-weekly gravity field solutions. However, as it is the case for GRACE-FO, MAGIC will suffer from temporal aliasing errors (Daras and Pail, 2017). Temporal aliasing could be solved by (1) improving background models or (2) ensuring that the gravity field can be recovered globally at sub-daily timescales with sufficient spatial resolution, for example, with a large constellation (Gunter et al., 2011). Reubelt et al. (2010) introduced the concept of multiple satellite missions to extend the spatio-temporal resolution beyond the Heisenberg sampling rule for a single gravitational functional. A special type of such mission concept are multiple pair constellations, that have gained increasing interest in recent years. They are a promising mission concept for daily and sub-daily gravity field recovery (e.g., Purkhauser and Pail, 2020; Pfaffenzeller and Pail, 2023).

One additional particularly important error source in the current ll-SST mission concept is the low-frequency accelerometer drift caused by uncontrollable thermal effects (Christophe et al., 2018), as well as the difficulty in accurately deriving calibration parameters. The latter effect results from the interplay between radiation pressure and aerodynamic forces modelling with poorly known surface properties, and their interaction with the satellite's complex geometry (Siemes et al., 2023). Although enhanced modelling aspects have recently been considered, such as the thermal emission from satellites (Hladczuk et al., 2025) and interaction with Earth's magnetic field (Jacobs et al., 2026), electrostatic accelerometers retain these fundamental limitations. One option to address them is to consider accelerometers based on the Cold Atom Interferometric (CAI) measurement concept, which has an intrinsic flat frequency spectrum (Malossi et al., 2010). With the development of CAI technology, potentially for and as a result of current efforts to deploy it in space (Lévèque et al., 2023), the ll-SST measurement concept is best suited to benefit from the extreme accuracy it may provide (Encarnação et al., 2026).

In the past, mission error analyses were conducted through full end-to-end simulation-based studies for GRACE (Kim and Tapley, 2002) and GRACE-FO (Loomis et al., 2011). Recently, similar studies have been conducted following the MAGIC mission concept (e.g., Pail et al., 2023; Daras et al., 2023b; Guo et al., 2024; Bender et al., 2025), as well as to analyse alternative mission concepts such as cartwheel formations or pendulum configurations, among others (e.g., Sharifi et al., 2007; Elsaka, 2014). They are also employed for mission analyses of multiple satellite missions (Reubelt et al., 2010; Gunter et al., 2011) and multiple pair constellations (Purkhauser and Pail, 2020; Pfaffenzeller and Pail, 2023; Zingerle et al., 2024; Kusche et al., 2025).

An alternative analytical approach to gravity field error analysis originated in the late 1980s. It employs Kaula's theory (Kaula, 1966) along with the Hill equations (Hill, 1878) to develop the observable signals into a Fourier series, so-called lumped series (Schrama, 1989). It builds upon the work of Colombo (1984), that refined the concept of ll-SST and introduced theoretical spectral considerations of satellite gravimetry, namely the Colombo-Nyquist rule, and the block-diagonal structure of the normal equations. Schrama (1990, 1991) provides a comprehensive formulation of the lumped coefficients for GNSS observations and gradiometers. Sneeuw (2000) expanded the methodology to inter-satellite ranging within the collinear formation. Li et al. (2016) developed the analytical observations for a pendulum formation. This methodology has been applied to the GOCE mission (Pail and Wermut, 2003) or in early studies of NGGM (Baldesarra et al., 2014), for example.

Another analytical approach, equivalent to the lumped coefficients theory, employs linear perturbation theory (Kaula, 1966) to convert the periodic variations in the orbital elements to position displacements (Rosborough and Tapley, 1987; Visser, 2005). Recently, it was employed for drag and attitude control analysis in the framework of NGGM (Cesare et al., 2022).

Full end-to-end simulation-based studies have become prominent in the design phase of operational missions, since they are comparatively more reliable and provide an end-to-end simulation framework that also serves as preparation for operational data processing. Nevertheless, the future of satellite gravimetry, with increasingly complex constellations, provides a context for leveraging the advantages of the analytical methodologies. MAGIC requires the definition of the inter-satellite nominal distance, the inclination for the 2nd pair, or the relative nodal separation. Applying optimisation techniques together with an end-to-end simulation is computationally expensive and requires the reduction of the search space (e.g.,Wiese et al., 2011; Ellmer, 2011; Pour et al., 2019). The analytical methodology significantly surpasses the simulation-based approach in computational efficiency, and it is well-suited to the optimisation challenges that the design of future missions encounters.

The analytical methodology however presents certain limitations. First, it relies on the assumption that the time-varying gravitational functionals considered as observations are periodic. This compromises the range of scenarios to be analysed. However, as long as no partial ground-track coverage is considered, the periodicity assumption is generally valid and does not have a major impact. The main disadvantage is the reliance on the assumption of stationary noise. As a result, errors in background models that cause temporal aliasing are disregarded, which is currently one of the major bottlenecks for better gravity field models.

In this paper, we apply the lumped coefficients theory to analyse the gravity field recovery capabilities from multiple pair constellations. Also, we introduce the repeating ground-track constraint in the lumped coefficients. The implementation is verified and validated with GRACE and GRACE-FO missions and limitations are identified. A special case for MAGIC is reproduced and analysed. Exploration of the full design space finds a global minimum in the co-optimization of the nominal separation and the second-pair inclination, and identifies key characteristics of the optimization landscape. To conclude this study, Cubesat performance is assumed to assess multiple pair constellations and their capability of computing daily and sub-daily gravity field solutions is evaluated.

2. Methodology

In this section, the mathematical foundations of the analytical error propagation methodology are described. This technique efficiently estimates the error characteristics of an estimated gravity field model. It accounts for the influence of the constellation and orbit geometry, a priori instrument error performance, and different observation types. In this study, we focus on ll-SST and multiple pair constellations.

2.1. The lumped series

The main idea consists of relating the spectral coefficients of an observable signal $f(t)$ to the gravity field. This is accomplished through the so-called lumped series, which arises when developing the gravity potential in terms of orbital elements and has the following form (Schrama, 1990).

$$f(t) = \sum_k \sum_m A'_{km} \cos\psi_{km} + B'_{km} \sin\psi_{km} \tag{1}$$

where m is the gravity field order, k is an index that arises from the series expansion, A'_{km}, B'_{km} represent an arbitrary set of lumped coefficients and ψ_{km} is the phase angle, which is defined from the orbital elements as:

$$\psi_{km} = k(\omega + M) + m(\Omega - \theta) = k\omega_o + m\omega_e \tag{2}$$

with ω the argument of perigee, M the mean anomaly, Ω the right ascension of the ascending node and θ the Earth Rotation Angle. They define the argument of latitude ω_o and the Earth-fixed longitude of the ascending node ω_e (see also Fig. 1). The orbital elements vary as the satellite

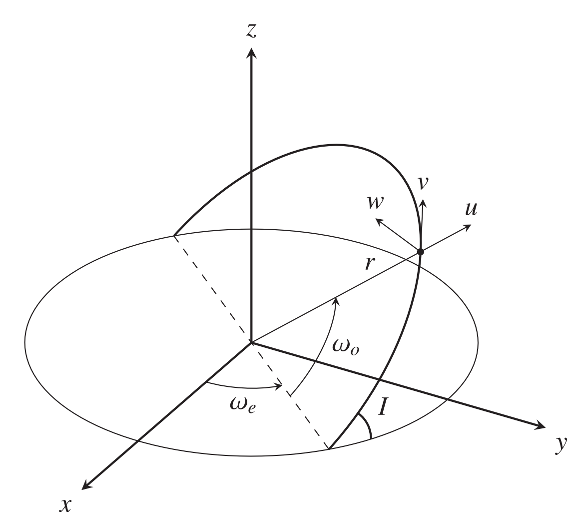

Fig. 1. Orbital variables and local orbital frame. Adapted from Balmino et al. (1996).

moves around the Earth, and so does the phase angle. Therefore, the time is implicitly included in the phase terms as:

$$\psi_{km} = \psi^0_{km} + \dot{\psi}_{km} t \tag{3}$$

where ψ^0_{km} is the initial phase and $\dot{\psi}_{km}$ is the orbital frequency. The initial phase terms can be computed from the initial orbital elements, while the associated frequencies are obtained from the secular rates of the orbital elements (Kaula, 1966).

$$\dot{\psi}_{km} = k\dot{\omega}_o + m\dot{\omega}_e \tag{4}$$

For the sake of simplicity, the initial phase term will not be considered hereafter.

$$f(t) = \sum_k \sum_m A_{km} \cos \dot{\psi}_{km} t + B_{km} \sin \dot{\psi}_{km} t \tag{5}$$

where A_{km}, B_{km} are an arbitrary set of lumped coefficients with zero initial phase. An initial phase angle can be considered for any lumped coefficients set provided hereafter through the rotation matrix below.

$$\begin{bmatrix} A_{km} \\ B_{km} \end{bmatrix} = \begin{bmatrix} \cos \psi^0_{km} & \sin \psi^0_{km} \\ -\sin \psi^0_{km} & \cos \psi^0_{km} \end{bmatrix} \begin{bmatrix} A'_{km} \\ B'_{km} \end{bmatrix} \tag{6}$$

2.2. The gravity potential

Earth's gravity field potential is typically expressed in terms of a series expansion of Spherical Harmonics (SH) (Heiskanen and Moritz, 1967).

$$V = \frac{\mu}{r} \sum_{l=0}^{L} \left(\frac{a_e}{r}\right)^l \sum_{m=0}^{l} \overline{P}_{lm}(\sin \phi) \left(\overline{C}_{lm} \cos m\lambda + \overline{S}_{lm} \sin m\lambda\right) \tag{7}$$

where l, m are the degree and order, a_e is the equatorial Earth radius, r the radial distance, ϕ the geocentric latitude, λ the geocentric longitude, L is the cut-off degree, $\overline{C}_{lm}, \overline{S}_{lm}$ are the fully-normalized Stokes coefficients, and $\overline{P}_{lm}$ are the fully-normalized associated Legendre polynomials.

To reformulate the potential in terms of orbital elements, the line potential assumption must be taken, i.e., the potential along the true orbit is approximated as the potential along a mean osculating ellipse. The resulting expression then takes the form of a lumped series. Assuming a circular reference orbit, each term of the expansion can be expressed as follows (Kaula, 1966).

$$V_{lm} = \frac{\mu}{r}\left(\frac{a_e}{r}\right)^l \sum_{\substack{k=-l \\ l-k=2p}}^{l} \overline{F}_{lmk}(I) \quad \left(\tilde{C}_{lm} \cos \psi_{km} + \tilde{S}_{lm} \sin \psi_{km}\right) \tag{8}$$

where I is the inclination of the orbital plane and p is an integer between 0 and L. Hence, the summation runs only through the k terms with same parity as l. The $\overline{F}_{lmk}(I)$ are the fully-normalized inclination functions, which are obtained from the Fast Fourier Transform (FFT) (Wagner, 1983). The coefficients $\tilde{C}_{lm}, \tilde{S}_{lm}$ relate to the fully-normalized Stokes coefficients as follows (Schrama, 1991).

$$\tilde{C}_{lm} = \begin{bmatrix} \overline{C}_{lm} \\ -\overline{S}_{lm} \end{bmatrix}_{l-m=\text{odd}}^{l-m=\text{even}} \qquad \tilde{S}_{lm} = \begin{bmatrix} \overline{S}_{lm} \\ \overline{C}_{lm} \end{bmatrix}_{l-m=\text{odd}}^{l-m=\text{even}}$$

The line potential formulation considers a mean semi-major axis, eccentricity and inclination, while the secular rates of the other orbital elements are assumed (e.g., Brouwer, 1959). Therefore, the phase term changes linearly in time as described by Eq. (3). Thus, the potential formulation in Eq. (7), that is defined in the spatial domain, is transformed to the time domain according to the mean satellite motion, resulting in the line potential as described by Eq. (8). Following the general lumped series expression in Eq. (1), it can be further transformed to the frequency domain through the lumped coefficients for the potential, shown below.

$$\begin{bmatrix} A_{km} \\ B_{km} \end{bmatrix} = \sum_{l=l_{min},2} \frac{\mu}{r}\left(\frac{a_e}{r}\right)^l \overline{F}_{lmk}(I) \begin{bmatrix} \tilde{C}_{lm} \\ \tilde{S}_{lm} \end{bmatrix} \tag{9}$$

The summation starts from $l_{min} = \max(|k|, m, 2) + \delta$ where $\delta = 0$ when $k - \max(|k|, m, 2)$ is even and $\delta = 1$ when it is odd.

2.3. The gravity observations

Lumped coefficients for the gravity vector can be computed in a local orbit reference frame through differentiation of the line potential (Koop, 1993; Balmino et al., 1996). The cross-track derivative avoids singularities in ω_o through some algebraic manipulation as described in Schrama (1989). In this work, they are expressed through cross-track inclination functions $\overline{F}^*_{lmk}(I)$ as defined by Balmino et al. (1996). The resulting lumped coefficients are shown below.

$$\begin{aligned} \begin{bmatrix} A^u_{km} \\ B^u_{km} \end{bmatrix} &= \sum_{l_{min},2} -(l+1)\frac{\mu}{r^2}\left(\frac{a_e}{r}\right)^l \overline{F}_{lmk}(I) \begin{bmatrix} \tilde{C}_{lm} \\ \tilde{S}_{lm} \end{bmatrix} \\ \begin{bmatrix} A^v_{km} \\ B^v_{km} \end{bmatrix} &= \sum_{l_{min},2} \frac{\mu}{r^2}\left(\frac{a_e}{r}\right)^l \overline{F}_{lmk}(I) \cdot k \begin{bmatrix} \tilde{S}_{lm} \\ -\tilde{C}_{lm} \end{bmatrix} \\ \begin{bmatrix} A^w_{km} \\ B^w_{km} \end{bmatrix} &= \sum_{l_{min},2} \frac{\mu}{r^2}\left(\frac{a_e}{r}\right)^l \overline{F}^*_{lmk}(I) \begin{bmatrix} \tilde{S}_{lm} \\ -\tilde{C}_{lm} \end{bmatrix} \end{aligned} \tag{10}$$

where u, v, w denote the radial, along-track and cross-track components (see Fig. 1).

2.4. The GNSS observations

To obtain a lumped series formulation for the position, the linearised dynamical model of the Hill equations is employed (Hill, 1878). For a non-resonant forcing term the system reads as:

$$
\begin{cases} \ddot{u} - 2n\dot{v} - 3n^2 u & = P_u \cos\omega t + Q_u \sin\omega t \\ \ddot{v} + 2n\dot{u} & = P_v \cos\omega t + Q_v \sin\omega t \\ \ddot{w} + n^2 w & = P_w \cos\omega t + Q_w \sin\omega t \end{cases} \tag{11}
$$

where ω is the forcing frequency and $P_{u,v,w}, Q_{u,v,w}$ represent the forcing amplitudes for the sine and cosine terms, which are given by the orbital frequency $\dot{\psi}_{km}$ and the lumped coefficients for the gravity vector $A^{u,v,w}_{km}, B^{u,v,w}_{km}$, respectively. In the left-hand side, n defines the mean motion. An analytical solution exists for non-resonant terms and gives rise to the GNSS observations in terms of lumped coefficients (Schrama, 1989). The linearity of the system in Eq. (11) allows for solving independently for every lumped series term.

$$
\begin{aligned}
\begin{bmatrix} A^{\Delta u}_{km} \\ B^{\Delta u}_{km} \end{bmatrix} &= \sum_{l_{\min},2} \frac{-(l+1)\dot{\psi}_{km} + 2nk}{\dot{\psi}_{km}\left(n^2 - \dot{\psi}^2\right)} \frac{\mu}{r^2}\left(\frac{a_e}{r}\right)^l \overline{F}_{lmk}(I) \begin{bmatrix} \tilde{C}_{lm} \\ \tilde{S}_{lm} \end{bmatrix} \\
\begin{bmatrix} A^{\Delta v}_{km} \\ B^{\Delta v}_{km} \end{bmatrix} &= \sum_{l_{\min},2} \frac{-(l+1)2n\dot{\psi}_{km} + k\left(3n^2 + \dot{\psi}^2_{km}\right)}{\dot{\psi}^2_{km}\left(n^2 - \dot{\psi}^2\right)} \times \\
&\quad \times \frac{\mu}{r^2}\left(\frac{a_e}{r}\right)^l \overline{F}_{lmk}(I) \begin{bmatrix} \tilde{S}_{lm} \\ -\tilde{C}_{lm} \end{bmatrix} \\
\begin{bmatrix} A^{\Delta w}_{km} \\ B^{\Delta w}_{km} \end{bmatrix} &= \sum_{l_{\min},2} \frac{1}{n^2 - \dot{\psi}^2_{km}} \frac{\mu}{r^2}\left(\frac{a_e}{r}\right)^l \overline{F}^{*}_{lmk}(I) \begin{bmatrix} \tilde{S}_{lm} \\ -\tilde{C}_{lm} \end{bmatrix}
\end{aligned} \tag{12}
$$

An important consideration is that resonant solutions arise when $\dot{\psi}_{km} = 0, \pm n$. They can however be disregarded for the analysis as is explained in Sneeuw (2000).

2.5. The ll-SST observations

The ll-SST concept employed in Gravity Research Missions (GRM) consists of two satellites flying along the same ground-track. By tracking the inter-satellite distance, the coefficients of the gravity field can be determined (Wolff, 1969). This mission concept is known as collinear, inline, leader–follower or GRACE-like formation.

Sneeuw (2000) formulated the lumped coefficients for a range observation in a collinear formation applying complex exponentials. Here, the same procedure is followed resulting in real-valued expressions instead, which simplifies the implementation avoiding the need to introduce complex number arithmetic. First, a first-order assumption is taken, thus approximating the range deviation $\Delta\rho(t)$ from the nominal separation ρ_0 as the projection along the line-of-sight (see Fig. 2).

$$
\Delta\rho(t) = \rho(t) - \rho_0 \approx \Delta\rho_x(t) \tag{13}
$$

Next, the local orbital frame displacements can be projected to the line-of sight. Therefore, only the radial and along-track components contribute to the linearised range observation.

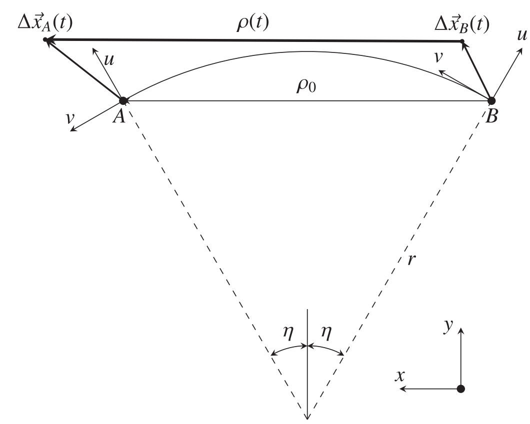

Fig. 2. Collinear formation. Adapted from Sneeuw, 2000.

$$
\Delta\rho_x = (\Delta u_A + \Delta u_B)\sin n\tau + (\Delta v_A - \Delta v_B)\cos n\tau \tag{14}
$$

with $\tau = \eta/n$ the nominal half-time of separation, η the half-angle separation, and u_A, u_B and v_A, v_B the radial and along-track displacements for the leading and trailing satellites, respectively. Introducing the lumped coefficients for the position displacements from Eq. (12) yields the lumped coefficients for the inter-satellite range observation.

$$
\begin{bmatrix} A^{\Delta\rho}_{km} \\ B^{\Delta\rho}_{km} \end{bmatrix} = \sum_{l_{\min},2} \frac{2\,\alpha_{lmk}}{\dot{\psi}^2_{km}\left(n^2 - \dot{\psi}^2_{km}\right)} \frac{\mu}{r^2}\left(\frac{a_e}{r}\right)^l \overline{F}_{lmk}(I) \begin{bmatrix} \tilde{C}_{lm} \\ \tilde{S}_{lm} \end{bmatrix} \tag{15}
$$

with

$$
\begin{aligned}
\alpha_{lmk} = &\left[-(l+1)\dot{\psi}_{km} + 2nk\right]\cos\left(\dot{\psi}_{km}\tau\right)\sin\tau + \\
&+ \left[2(l+1)n\dot{\psi}_{km} - k\left(3n^2 + \dot{\psi}^2_{km}\right)\right]\sin\left(\dot{\psi}_{km}\tau\right)\cos\tau
\end{aligned}
$$

Lumped coefficients for the range-rate and range-acceleration observations can be obtained differentiating in the frequency domain.

$$
\begin{bmatrix} A^{\Delta\dot{\rho}}_{km} \\ B^{\Delta\dot{\rho}}_{km} \end{bmatrix} = \dot{\psi}_{km} \begin{bmatrix} B^{\Delta\rho}_{km} \\ -A^{\Delta\rho}_{km} \end{bmatrix} \tag{16}
$$

$$
\begin{bmatrix} A^{\Delta\ddot{\rho}}_{km} \\ B^{\Delta\ddot{\rho}}_{km} \end{bmatrix} = -\dot{\psi}^2_{km} \begin{bmatrix} A^{\Delta\rho}_{km} \\ B^{\Delta\rho}_{km} \end{bmatrix} \tag{17}
$$

Operationally, low-pass filters are applied to suppress high-frequency noise (Wu et al., 2006). Such a low-pass filter can be also applied in the lumped coefficients. Nonetheless, its impact on the quality of the retrieved gravity field solution is negligible, since the gravity field signal significantly drops for higher frequencies, e.g., over 30 mHz (Abich et al., 2019).

2.6. Error propagation

The linear assumptions taken have allowed for relating linearly the observations in terms of lumped coefficients to the parameters to be estimated, i.e. the Stokes coefficients.

$$\bar{y} = H\bar{x} + \bar{e} \tag{18}$$

with $\bar{y}$ the observation vector, H the design matrix, $\bar{x}$ the parameter vector and $\bar{e}$ the vector of residuals. An observation covariance P_{yy} can be propagated to the parameters.

$$P_{xx} = \left(H^T P_{yy}^{-1} H + P_{cc}^{-1}\right)^{-1} = N^{-1} \tag{19}$$

where N is the normal matrix, its inverse, P_{xx} is the parameter covariance and P_{cc} is an a priori covariance that can be employed to constrain the parameters. In this way, system noise translates to error of the computed gravity field solutions.

Assuming that the inter-satellite range measurement consists of a wide-sense stationary process, the covariance function is time independent and the observation covariance is block-Toeplitz in the time domain (Ellmer, 2018). Under the Discrete Cosine Transform, in the frequency domain, such a matrix becomes diagonal. This is the assumption taken for the observation covariance of the lumped coefficients. The associated variance for each spectral line is computed from the power spectral density of the observation signal (Sneeuw, 2000).

$$\sigma_{km}^2 = \int_{f_{km}-\Delta f/2}^{f_{km}+\Delta f/2} S(f)\,df \approx S(f)\Delta f \tag{20}$$

with $f_{km} = \dot{\psi}_{km}/2\pi$ the linear frequency, $\Delta f = 1/T$ the frequency resolution, T the observation time, and $S(f)$ the power spectral density. For every pair of lumped coefficients in the observation vector, there are two associated entries in the diagonal of the observation covariance given by σ_{km}^2.

The diagonal observation covariance and the structure of the lumped coefficients result in a block-diagonal structure of the normal matrix when grouping terms with the same order together (Colombo, 1984). This reduces the time complexity of the problem from $\mathcal{O}(L^6)$ to $\mathcal{O}(L^4)$.

2.7. Observability of the orbital frequencies

According to the Shannon-Nyquist sampling theorem, the sampling frequency $f_s = 1/T_s$ defines a maximum resolvable frequency of an observed discrete signal given by the Nyquist frequency $f_N = 2f_s = 2/T_s$. Therefore, the lumped coefficients associated with higher frequencies cannot be observed and they fold into the lower part of the spectrum. In this work, the undersampled lumped coefficients are simply neglected and not employed for covariance propagation (Sneeuw, 2000). Operationally, considering typical resampling frequencies around $f_s = 0.2\,\mathrm{Hz}$ (e.g., Ellmer, 2018), this is a valid assumption because the power of the temporal gravity field signal significantly decays at such higher frequencies (Abich et al., 2019).

2.8. The repeating ground-track constraint

The intrinsic formulation of the lumped series resembling a Fourier series requires a periodicity condition of the signal considered, or in this case, of the ground-track described. This constrains the values of the lumped series frequencies. There exists a commensurability relation, here depicted through integer frequencies, which can be interpreted as cycles per ground-track repeatability period.

$$\gamma_{km} = \frac{N_r}{\dot{\omega}_o}\dot{\psi}_{km} = kN_r - mN_d \tag{21}$$

with N_r the number of orbital revolutions and N_d the nodal days of the repeating orbit. If the k, m indices are allowed to take sufficiently high values, i.e., the cut-off degree is sufficiently high, some frequencies overlap (Schrama, 1990).

$$\gamma_{k_1m_1} = -\gamma_{k_2m_2} \tag{22}$$

This gives rise to the so-called Colombo-Nyquist rule for satellite gravimetry: the maximum resolvable gravity field degree for a polar orbit was determined to $L = N_r/2$ (Colombo, 1984). However, Visser et al. (2012) indicated that this condition only guarantees the longitude homogeneity of the quality of the recovered gravity field. The frequency overlap in Eq. (22) is non-degenerate, i.e., the linear system can still be solved. The condition for ill-posedness is simply the following:

$$\gamma_{k_1m_1} = \gamma_{k_2m_2} \tag{23}$$

The maximum resolvable degree is therefore $L = N_r$ (Visser et al., 2012). At this point, the space of orbital frequencies is full for the considered repeating ground-track. Thus, increasing the cut-off degree leads to an overparametrization, and the system becomes ill-posed. Additional observation types allow for resolving higher degrees. Given j the number of different observation types, the maximum resolvable degree becomes $L = j \cdot N_r$ for a polar orbit (Visser et al., 2012). Additional observations on inclined orbits relax this condition even further, as condition number analysis shows in Valles-Valverde (2025).

For this work, it is paramount to take the overlapping between frequencies into account. Although the non-degenerate frequency overlap does not result in ill-posedness of the problem, it combines certain lumped coefficients from different orders under the same frequencies. Therefore, correlations between them are introduced, resulting in a normal matrix that exhibits a characteristic block pattern (Visser et al., 2012) (see Fig. 3). Correlated blocks are computed from:

$$m = (-1)^n \cdot m_0 + N_r\left\lceil\frac{n}{2}\right\rceil \tag{24}$$

with m_0 the block base order and $n = 0, 1, \ldots$ as long as $m \leqslant L$. The system can similarly be solved in a block-wise approach for every block base order.

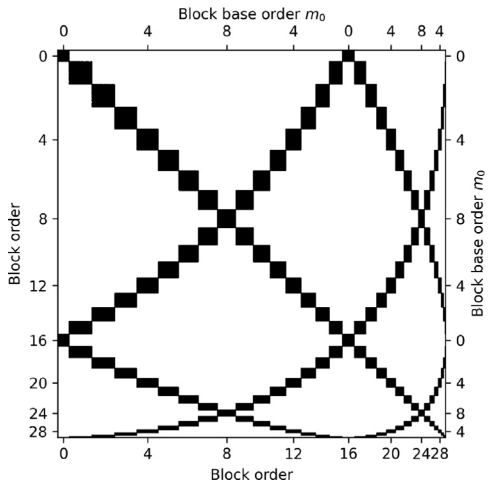

Fig. 3. Block structure of the normal matrix: $N_r = 16$.

2.9. Application to multiple pair constellations

Multiple pair constellations can be modelled depending on the type of configuration selected. Two different cases must be distinguished depending on whether the pairs fly over the same ground-track or a different one.

Multiple pairs might fly over the same ground-track to cover it in a lower amount of time than its repeatability period. This allows for sub-daily gravity field solutions. Essentially, if the gravity field remained static within the observation period, the quality of the recovered solution could be assumed to be equivalent to a single satellite covering the whole ground-track. As a result, a single pair of lumped coefficients is considered for every sampling frequency. A subtle difference is that the observations of different satellites are uncorrelated. Therefore, the combined set of measurements over the orbital frequency spectra has a PSD that flattens out below a cut-off frequency given by the observation period. Further implications and operational handling of a non-static true gravity field are discussed in Section 3.5.

On the other hand, multiple pairs flying over different ground-tracks add more information to the system. This can be accounted for by accumulating the normal equations for every ground-track, assuming uncorrelated observations between satellite pairs. Different observation types, such as GNSS and ll-SST observations, can be combined following the same approach.

3. Error sources

The error sources in a gravimetric mission are numerous (e.g., Kim and Tapley, 2002). To properly estimate the resulting error in the gravity field coefficients, it is important to identify the dominant effects. In this work, the ranging system instrument, the accelerometer, attitude noise and GNSS errors are considered.

3.1. Inter-satellite ranging system

Two different ranging systems are employed for ll-SST: a Microwave Ranging Instrument (MWI) or a Laser Ranging Instrument (LRI). The former allows for more relaxed attitude pointing requirements, while the latter typically has a lower noise floor. Their error is associated with the ll-SST observations lumped coefficients, as described in Section 2.5.

3.2. Accelerometers

The accelerometers are crucial to measure non-gravitational forces such as drag or radiation pressure with sufficient accuracy. They are integrated along with gravitational accelerations to obtain the satellite positions and, in turn, to model the range observations (e.g., Mayer-Gürr, 2006). Hence, accelerometer errors propagate to the observations, thus biasing the low frequencies (see Fig. 5).

The lumped coefficients of the accelerations in the local orbital frame were presented in Section 2.3. First, they can be related to the position lumped coefficients as:

$$\begin{aligned}
\begin{bmatrix} A^{\Delta u}_{km} \\ B^{\Delta u}_{km} \end{bmatrix} &= \frac{1}{\dot{\psi}_{km}\left(n^2-\dot{\psi}^2_{km}\right)} \begin{bmatrix} A^{u}_{km} & -B^{v}_{km} \\ B^{u}_{km} & A^{v}_{km} \end{bmatrix} \begin{bmatrix} \dot{\psi}_{km} \\ 2n \end{bmatrix} \\
\begin{bmatrix} A^{\Delta v}_{km} \\ B^{\Delta v}_{km} \end{bmatrix} &= \frac{1}{\dot{\psi}^2_{km}\left(n^2-\dot{\psi}^2_{km}\right)} \begin{bmatrix} B^{u}_{km} & A^{v}_{km} \\ -A^{u}_{km} & B^{v}_{km} \end{bmatrix} \begin{bmatrix} 2n\dot{\psi}_{km} \\ 3n^2+\dot{\psi}^2_{km} \end{bmatrix} \\
\begin{bmatrix} A^{\Delta w}_{km} \\ B^{\Delta w}_{km} \end{bmatrix} &= \frac{1}{n^2-\dot{\psi}^2_{km}} \begin{bmatrix} A^{w}_{km} \\ B^{w}_{km} \end{bmatrix}
\end{aligned} \tag{25}$$

In this way, the accelerometer errors are propagated to position errors that can be incorporated to the lumped coefficients of the GNSS observations from Section 2.4. Furthermore, the lumped coefficients of the position observation relate to the range observation ones as follows:

$$\begin{bmatrix} A^{\Delta\rho}_{km} \\ B^{\Delta\rho}_{km} \end{bmatrix} = \begin{bmatrix} \cos\dot{\psi}_{km}\tau & \sin\dot{\psi}_{km}\tau \\ -\sin\dot{\psi}_{km}\tau & \cos\dot{\psi}_{km}\tau \end{bmatrix} \begin{bmatrix} A^{\Delta u}_{km} & A^{\Delta v}_{km} \\ B^{\Delta u}_{km} & B^{\Delta v}_{km} \end{bmatrix} \begin{bmatrix} \sin\eta \\ \cos\eta \end{bmatrix} \tag{26}$$

Thus, accelerometer errors can be propagated to range observation errors and incorporated to the range observation described in Section 2.5.

According to the derived expressions, integration of the accelerometer noise blows up around the orbital frequency because of resonant solutions for the linearised dynamics. This gives rise to a peak in the observation noise at the orbital frequency (see Fig. 5).

3.3. Antenna offset centre correction

The range observation between both satellites does not consist of the distance between the satellite centres of mass, but rather between the antenna centres. The Antenna Offset Centre (AOC) correction accounts for this mismatch

(Kim and Tapley, 2002), projecting the antenna offset centre vectors $\bar{c}_A, \bar{c}_B$ along the nominal line-of-sight (see Fig. 4).

$$\Delta\rho^{\mathrm{AOC}} = ||\bar{c}_A|| \cos\beta_A + ||\bar{c}_B|| \cos\beta_B \tag{27}$$

For this purpose, information on the deviation from the nominal attitude β is required. As a consequence, attitude errors propagate to the inter-satellite range observations. The spectra can be propagated through a first-order assumption on the cosine term.

$$\cos\beta(t) = \cos(\beta_0 + \Delta\beta(t)) \approx \cos\beta_0 - \sin\beta_0 \Delta\beta(t) \tag{28}$$

with β_0 the mean deviation angle and $\Delta\beta(t)$ the time-varying zero-mean component. Thus, the lumped coefficients of the deviation angle relate to the antenna centre offset ones as shown below.

$$\begin{bmatrix} A^{\rho}_{km} \\ B^{\rho}_{km} \end{bmatrix} = -||\bar{c}_A|| \sin\beta_{A,0} \begin{bmatrix} A^{\beta_A}_{km} \\ B^{\beta_A}_{km} \end{bmatrix} - ||\bar{c}_B|| \sin\beta_{B,0} \begin{bmatrix} A^{\beta_B}_{km} \\ B^{\beta_B}_{km} \end{bmatrix} \tag{29}$$

Consequently, attitude noise can be propagated to the ll-SST observations from Section 2.5.

The attitude knowledge is generally determined from sensor fusion of star cameras, that provide long-term stability, and gyroscopes or accelerometers, with lower high-frequency noise (e.g., Bandikova, 2015). The data fusion can be conducted in the frequency domain leveraging the diagonal assumption for the observation covariance. For this purpose, the variance of angular rate or angular rate acceleration is propagated through integration in the frequency domain. The variance reduction follows from the optimal combination of two independent observations. For example, gyroscope and star camera fusion errors can be computed as:

$$\sigma^2_{km,\hat{\theta}} = \frac{1}{\dfrac{1}{\sigma^2_{km,\theta}} + \dfrac{\dot{\psi}^2_{km}}{\sigma^2_{km,\dot{\theta}}}} \tag{30}$$

An important consideration regarding the antenna offset centre correction is that errors are no longer stationary. This arises because (1) the standard deviation of the AOC correction is proportional to the nominal deviation angle and (2) attitude data is heteroscedastic due to Sun/Moon blinding of star cameras. For this work, the effect of non-stationary errors in the AOC correction is neglected given their low impact on the GRACE mission (Ellmer, 2018).

3.4. GNSS errors

GNSS observations are employed to obtain kinematic orbits. They serve as observations to compute a dynamic orbit, thus fixing to space the integrated accelerations. In this procedure, they are also employed to evaluate the gravitational accelerations from background models. Furthermore, the dynamic orbits allow for the computation of the normal equations for the range observations. The current accuracy of GNSS in Low Earth Orbit (LEO), in the cm level (e.g., Luo et al., 2022), is assumed sufficient to neglect the impact of GNSS errors on the range observation model.

Nonetheless, kinematic orbits themselves can be employed as observations to retrieve information on the gravity field. One example is GRACE monthly solutions. Kinematic orbits are combined with inter-satellite range observations to improve the quality of the monthly gravity field solutions (Mayer-Gürr, 2006). In this work, kinematic orbit errors are assumed white noise with 4 cm for a sampling frequency of 1 Hz, following a survey on GNSS accuracy for GRACE-FO mission (Luo et al., 2022). This value might be conservative, but temporal correlations arise because of various reasons, namely ambiguity resolution or constellation geometry (Jäggi et al., 2011). As a result, the lower part of the frequency error spectrum is degraded. In this way, definition of a PSD model for the kinematic orbit errors is not trivial.

Lastly, when applied to gravity field determination, GNSS observations suffer from low-frequency noise due to error propagation from accelerometers when computing the dynamic orbit. This can be incorporated into the lumped coefficients observations from Section 2.4, following the propagation from the acceleration lumped coefficients (see Section 3.2).

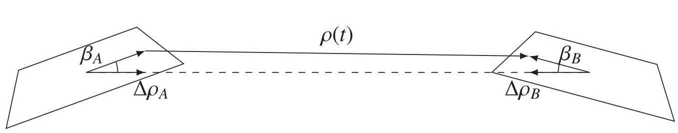

Fig. 4. Antenna centre offset correction.

3.5. Background model errors

One of the main limitations observed in satellite gravimetry is associated with background models. On the one hand, tidal effects are modelled and reduced to retrieve the non-tidal signal. Nonetheless, they are inaccurate and can contaminate the solution (e.g., Knudsen and Andersen, 2002). Moreover, undersampled short-term variations of the non-tidal components can leak power to the mean monthly solutions. De-aliasing models are employed to reduce these contributions from the observations, but these models also present errors that remain as residual signals. There exist mitigation strategies such as co-estimation of daily lower-order gravity fields (Wiese et al., 2011) or introducing a priori covariance information to constrain the daily variability of the gravity field (Kvas and Mayer-Gürr, 2019). Despite them, temporal aliasing remains one of the major error sources in Earth's gravity field monitoring.

Background models error have not been taken into account for this work. While they are among the main error sources for GRACE, GRACE-FO and upcoming MAGIC, they could be circumvented with large constellations that observe the low order sub-daily gravity field variations. For example, Pfaffenzeller and Pail (2023) demonstrates that multiple pair constellations are significantly less affected by temporal aliasing. Since this work ultimately analyses multiple pair constellations for daily and sub-daily gravity field, we do not consider these error sources.

4. Results

In this section, different missions are analysed with their associated instrument spectra. First, GRACE/GRACE-FO mission errors are compared with operational results to assess the validity of the methodology. Special attention is drawn to the solution from September 2004, where the mission fell into the $N_\mathrm{r}/N_\mathrm{d} = 61/4$ resonance. Subsequently, the suitability for preliminary mission design is demonstrated with the MAGIC mission to define global optimal values for the nominal separation as well as the inclination of the second pair. Lastly, multiple pair constellations for daily and sub-daily gravity field retrieval are studied.

4.1. GRACE/GRACE-FO mission

The ranging measurements were conducted by means of a K-Band Ranging (KBR) instrument for GRACE mission. GRACE-FO employed an identical instrument, and also carried a LRI for technology demonstration purposes. Currently, fuel saving activities to extend mission lifetime have required coarse pointing mode. Therefore, the LRI is no longer operational. The amplitude spectral density (ASD) for KBR is taken from Kornfeld et al. (2019).

$$A_{\rho_\mathrm{KBR}}(f) = 2.62 \cdot \sqrt{1 + \left(\frac{0.003}{f}\right)^2} \frac{\mu\mathrm{m}}{\sqrt{\mathrm{Hz}}} \tag{31}$$

with f the frequency in Hz for every ASD expression throughout this work. The ASD is expressed in units/$\sqrt{\mathrm{Hz}}$. In this way, it accounts for the variance correction in the time domain from signal resampling, e.g., a lower sampling frequency resulting from a longer averaging period implies lower noise.

The accelerometers employed were the SuperSTAR and SuperSTAR-FO accelerometers respectively. The latter is an improved version of the former but its performance is essentially the same. The ASD for the along-track and radial directions are given in Christophe et al. (2015) as:

$$A_{\ddot{u}}(f) = A_{\ddot{v}}(f) = 0.1 \cdot \sqrt{1 + \left(\frac{f}{0.5}\right)^4 + \frac{0.005}{f}} \frac{\mathrm{nm}}{\mathrm{s}^2\sqrt{\mathrm{Hz}}} \tag{32}$$

The cross-track acceleration is assumed ten times worse. Furthermore, for GRACE-FO and the last months of GRACE mission, one of the accelerometers is not working and an accelerometer transplant is required. Therefore, the observation noise of the satellite receiving the transplant is larger. Murböck et al. (2023) analyses the residual of the transplanted accelerations and shows a degradation of the accelerometer noise of roughly one order of magnitude, also depending on the solar cycle phase.

Regarding attitude noise, for the GRACE mission, angular acceleration errors are taken from Klinger (2018):

$$A_{\ddot{\theta}}(f) = 5 \cdot 10^{-6} \sqrt{1 + \frac{0.01}{f}} \frac{\mathrm{rad}}{\mathrm{s}^2\sqrt{\mathrm{Hz}}} \tag{33}$$

For the GRACE-FO mission, the ASTRIX 120 3-axis fiber-optic gyroscope provides angular velocity measurements with a white noise component (Goswami et al., 2021) and random walk noise component due to bias stability contribution (Airbus Defence and Space, 2022):

$$A_{\dot{\theta}}(f) = 6.6 \cdot 10^{-7} \sqrt{1 + \left(\frac{8.7 \cdot 10^{-4}}{f}\right)^2} \frac{\mathrm{rad}}{\mathrm{s}\sqrt{\mathrm{Hz}}} \tag{34}$$

Lastly, the GRACE-FO star camera solution is assumed to have a constant Allan deviation, and the following spectral characteristics (Goswami et al., 2021):

$$A_{\theta}(f) = \frac{8.5 \cdot 10^{-6}}{\sqrt{f}} \frac{\mathrm{rad}}{\sqrt{\mathrm{Hz}}} \tag{35}$$

The GRACE-FO mission carries three star cameras onboard. At least two star cameras are available most of the time, thus compensating for the anisotropic error along the bore-sight axes. For GRACE mission, roughly 25% of the time only one camera is available, which degrades the error in the nominal angular deviation. The PSD is not the right tool to account for this non-stationary behaviour, as previously discussed. As a trade-off, given the minor impact on the gravity field quality (e.g., Ellmer, 2018), and considering empirical analysis (not shown), this works assumes a star camera performance for GRACE six times worse than the employed for GRACE-FO.

An overview of the contributions of every error source to the range-rate is shown in Figs. 5 for GRACE-FO with wide pointing mode, i.e. $\beta_0 \approx 2^\circ$. The total range-rate error (black) differs from post-fit residuals obtained operationally (gray), with better operational performance of the KBR instrument and slightly larger errors roughly in the 0.1–3 mHz frequency band. As previously discussed, there exist degraded accelerometer measurements as well

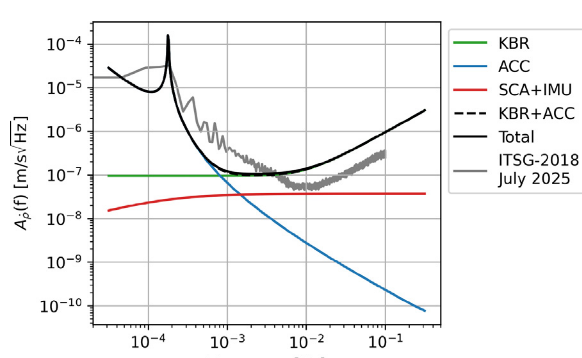

Fig. 5. GRACE-FO mission range-rate ASD (wide-pointing).

as unmodelled error sources, namely background model errors (see Section 3.5).

4.1.1. Non-resonant solution

The analytical results are compared to the ITSG-2018 gravity field solutions from TU Graz (Mayer-Gürr et al., 2018; Kvas et al., 2019). For this purpose, the RMS per coefficient per degree is employed (Heiskanen and Moritz, 1967).

$$\delta_l = \sqrt{\frac{1}{2l+1}\sum_{m=0}^{l}\sigma^2\left(\overline{C}_{lm}\right) + \sigma^2\left(\overline{S}_{lm}\right)} \qquad (36)$$

In this section, a cut-off degree of $L = 96$ is selected to allow for comparison with the normal equations provided by ITSG-2018 solutions.

First, the monthly solution of July 2025 for GRACE-FO is arbitrarily chosen given the good operational quality of the solution. The RMS degree spectra are shown in Fig. 6. The analytical model underestimates the ITSG-2018 commission error (black dashed) roughly up to a factor of three for ll-SST only solutions (blue) and a factor of six for ll-SST + GNSS solutions (red). The differences with the ITSG-2018 results are expected: the instrument error noise model biases the estimated error performance, while there exist (1) a disagreement with ITSG-2018 residuals and (2) unmodelled error sources, as previously discussed (see Section 3.5). For example, considering the accelerometer performance suggested by Murböck et al. (2023), the analytical method (green) yields very similar results to ITSG-2018 solution.

Gravity field error in the SH spectrum can be projected to the spatial domain, for example, in terms of Equivalent Water Height (EWH) (Wahr et al., 1998). Figs. 7 and 8 show the homogeneity in longitude of the recovered field for both the ITSG-2018 solution and the analytical commission errors, respectively. While this resembles a zonal coefficients pattern, this is in fact associated with the m-block-diagonal structure of the parameter covariance, which strictly leads to longitude invariance of the spatial error pattern (see Appendix B.2 in Sneeuw, 2000 for a detailed proof). The m-block-diagonal structure occurs because the Colombo-Nyquist criteria is fulfilled and no counter-diagonals arise (Visser et al., 2012), as discussed in Section 2.8. The analytical model also captures the error differences with latitude. Given the polar orbits, more samples per unit area are taken near the poles, and thus these regions show lower errors. The mismatch in the scaling occurs because of differences at higher degrees that dominate the EWH spectrum.

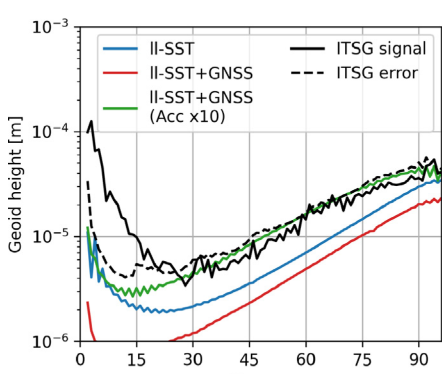

Fig. 6. Degree RMS. GRACE-FO mission analytical vs. ITSG-2018: July 2025.

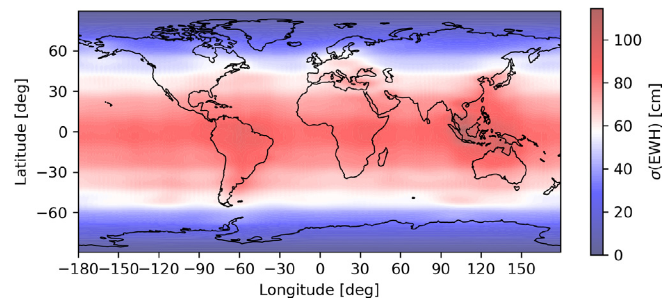

Fig. 7. ITSG-2018 EWH error synthesis: July 2025.

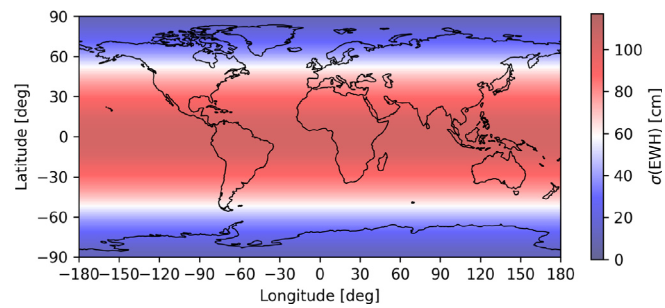

Fig. 8. Analytical EWH error synthesis: July 2025.

4.1.2. Resonant solution

Next, the solution from September 2004 is studied. GRACE mission fell into a $N_r/N_d = 61/4$ resonance[1] that significantly degraded the gravity field quality (e.g., Klokocník et al., 2008). From the analytical point of view, for such a ground-track, a gravity field can only be resolved up to $L = 61$, although aliasing is still embedded (see Section 2.8). Nonetheless, adding more observation types increases the maximum resolvable degree (Visser et al., 2012). Hence, higher degrees can be solved combining range-rate and GNSS observations. In spite of this, the analytical model yields unrealistically high values, especially for high-degree coefficients. Operationally, constraints are also applied through background models. Moreover, the satellites do not perfectly fly along the resonant orbit, thus relaxing the degradation in the quality of the operational ITSG-2018 solution. Therefore, one must be careful when comparing analytical to operational results. For this reason, a Kaula-type constraint (Kaula,

[1] LEO resonant orbits are shown in Fig. 19, Section 4.3

1959) has been applied, finding the best agreement for a Kaula constant of $K = 10^{-6}$ (see Fig. 9).

The degree spectrum for the discussed resonant solution is shown in Fig. 9. The quality of ITSG-2018 solution is degraded compared to the non-resonant case (black dashed) (cf. Fig. 6), which is also captured by the analytical methodology (red). For both cases, the spectra shifts upwards, especially for higher degrees.

Analogously to the non-resonant case, SH errors are projected to the spatial domain as EWH in Figs. 10 and 11 for ITSG-2018 solution and the analytical methodology, respectively. ITSG-2018 solution depicts a characteristic striped pattern that is also predicted by the analytical methodology, as a consequence of the repeating ground-track constraint. Validating that the analytical methodology properly captures this behaviour is crucial for future missions where resonances are not avoided but leveraged instead.

4.2. MAGIC mission

MAGIC mission aims at improving spatial and temporal resolution of gravity field solutions. For this purpose, two satellite pairs will fly in a polar and an inclined orbit, GRACE-C and NGGM (Daras et al., 2023a) respectively. Among the possible selected orbits in LEO (see Fig. 19, Section 4.3), this section optimizes the particular case for a repeating orbit with $N_\mathrm{r}/N_\mathrm{d} = 76/5$, which represents a trade-off in orbit height between gravity field attenuation, mission lifetime, and the possibility to fly drag-free, among others (Bender et al., 2025). The resonant parameters define the same nodal precession for both satellites pairs. To achieve the desired rates, given their different inclinations, they have different orbit altitudes.

As a consequence of the orbit selection, the constellation repeats every five nodal days, which defines the temporal resolution. For this work, the spatial resolution is defined from the degree at which the signal-to-noise ratio approaches one. However, in practice, if the signal power is higher at certain Earth locations, insights can be derived from higher degrees, i.e., lower spatial scales. A rule of

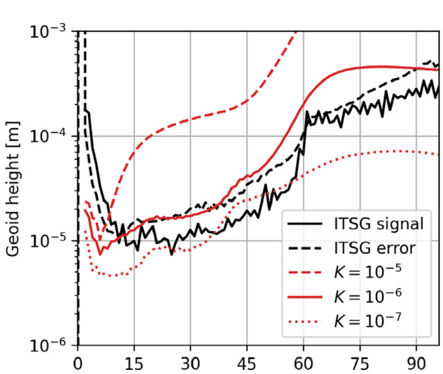

Fig. 9. Degree RMS. GRACE mission analytical vs. ITSG-2018: September 2004.

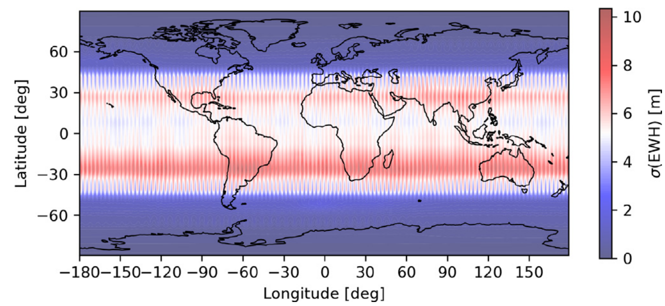

Fig. 10. ITSG-2018 EWH error synthesis: September 2004.

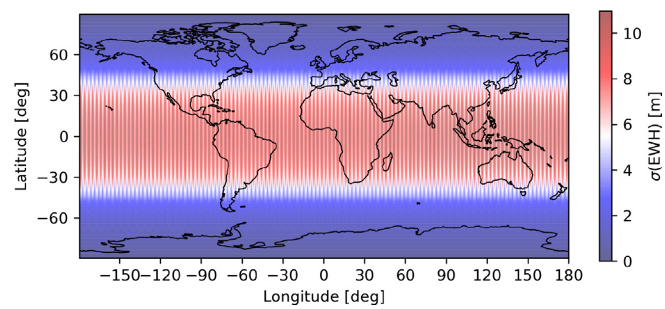

Fig. 11. Analytical EWH error synthesis: September 2004.

thumb for the spatial scale can be computed from the half-wavelength of the respective degree (e.g., Rummel et al., 2002). For example, for GRACE/GRACE-FO, the noise contaminates the signal starting at $l \sim 30$, i.e. roughly 700 km. This results in the characteristic striping patterns in the monthly solutions (not to be confused with the stripes in commission errors due to resonance).

To attain a better spatial resolution, one shall therefore improve the instruments performance to achieve lower noise in the SH spectrum. For this purpose, NGGM will carry (1) on-board MicroSTAR accelerometers with lower noise floor (Christophe et al., 2018), (2) a drag-free compensation system to ensure that the measured accelerations lie within the accelerometer dynamic range (Cesare et al., 2022), and (3) a laser tracking instrument (LTI) with much lower noise than a KBR instrument as the main and only source for ll-SST observations (Nicklaus et al., 2022). Alternatively, GRACE-C will rely on instrument heritage from GRACE-FO, thus employing the same LRI as well as the SuperSTAR-FO accelerometers (Pail et al., 2023).

In this section, we employ the instrument noise specifications as provided by the ESA/NGGM Science Study (Pail et al., 2023), to allow for consistent comparison. An overview in terms of range-rate noise ASD is shown in Fig. 12 for both GRACE-C and NGGM.

The mission requires the selection of an optimal inclination of the second pair as well as a suitable value for the nominal inter-satellite distance. Another parameter to be defined is the relative separation of the ascending nodes between the satellite pairs. A detailed analysis can be found in Valles-Valverde (2025), where it is concluded that interleaving ground-tracks at the equator can lead up to 10%

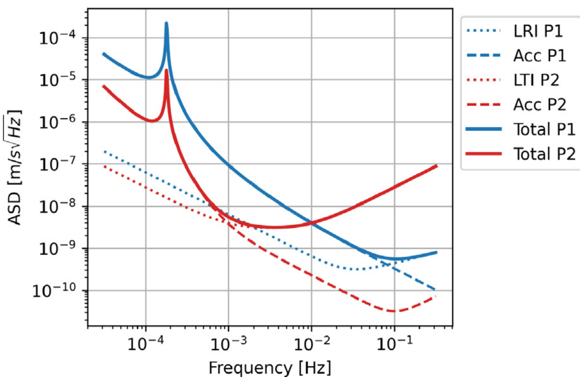

Fig. 12. MAGIC mission range-rate ASD. Adapted from Pail et al. (2023).

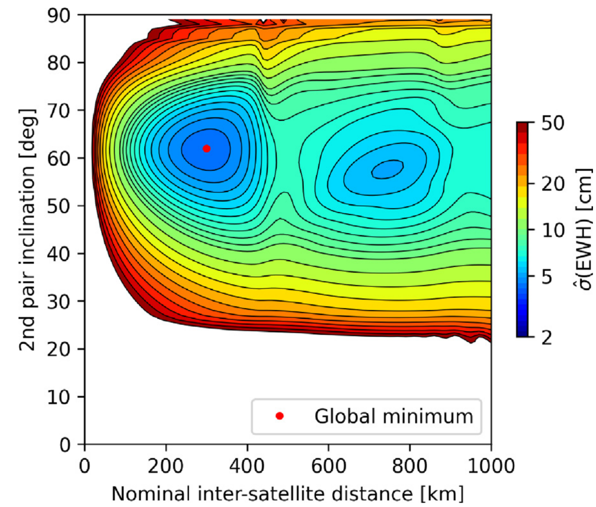

Fig. 13. MAGIC mission optimization design space for $N_r/N_d = 76/5$.

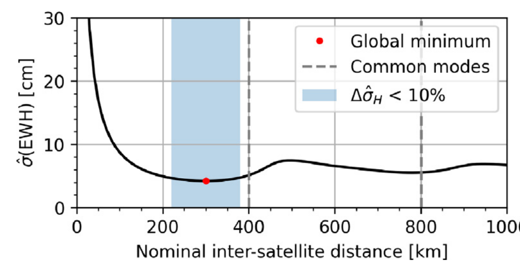

Fig. 14. MAGIC optimal solution sensitivity to nominal separation.

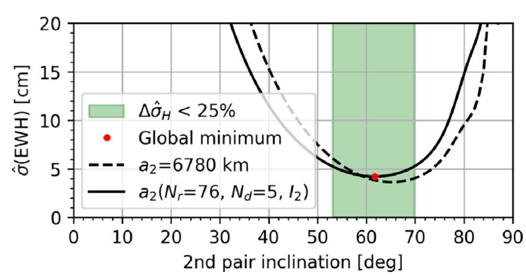

Fig. 15. MAGIC optimal solution sensitivity to second-pair inclination.

improvement in degree amplitudes, value that decays the denser the ground-track. Therefore, this ground-track separation policy is assumed.

To define the optimization problem, a cost function is chosen as the average on the sphere of the EWH standard deviation $\hat{\sigma}_H$.

$$\hat{\sigma}_H^2 = \frac{1}{4\pi a_e^2} \int_\Omega \sigma_y^2(\lambda, \phi)\, d\Omega \tag{37}$$

Application of spherical harmonics orthogonal properties and the normalization employed significantly simplify this integral (e.g., Haagmans and van Gelderen, 1991).

$$\hat{\sigma}_H = \frac{a_e \rho_e}{3\rho_w} \sqrt{\sum_{l=2}^{L} \left(\frac{2l+1}{1+k_l'}\right)^2 \sum_{m=0}^{l} \left(\sigma^2(\overline{C}_{lm}) + \sigma^2(\overline{S}_{lm})\right)} \tag{38}$$

with $\rho_e = 5300\,\mathrm{kg/m^3}$ and $\rho_w = 1000\,\mathrm{kg/m^3}$ the average Earth and water densities, and k_l' the elastic Love numbers (Wahr et al., 1998). In this way, expensive global covariance propagation is avoided and the whole design space can be quickly explored, thus guaranteeing a global optimal solution.

Fig. 13 shows the design space for optimization of nominal ranging distance and inclination of the second pair.

The optimal solution has been determined to be $I_2 = 61.5^\circ$ and $\rho_0 = 297\,\mathrm{km}$. The sensitivity of the optimal solution to every design variable is shown in Figs. 14 and 15. Fig. 14 shows an oscillatory behaviour, the so-called common mode attenuation (Wolff, 1969). Sneeuw (2000) relates the cut-off degree and the inter-satellite distance for every mode.

$$\rho_0 = \frac{2\pi a_e i}{L} \tag{39}$$

where i denotes the i-th mode.

The appearance of the common modes is indicated in Fig. 14 accordingly. The zeroth mode occurs at $\rho_0 = 0\,\mathrm{km}$. Hence, it cannot be avoided. The optimal solution is found before the first mode. The optimal nominal separation is higher than values chosen in mission design studies (e.g., Daras et al., 2023b; Bender et al., 2025). However, the cost function is rather flat around the global minimum. Hence, suggested values around $\rho_0 \approx 220\,\mathrm{km}$ would not imply a significant increase in the average error (around 10%), and might be beneficial, for instance, from the point of view of formation stability.

Regarding the inclination of P2, Bender et al. (2025) choose $I_2 = 75^\circ$ and ESA/NGGM Science Study claims that the optimal value is found between 65° to 75° (Pail et al., 2023). We however find a lower optimal value at $I_2 = 61.5^\circ$, which is close to the original $I_2 = 63^\circ$ proposed by Bender et al. (2008). Slightly higher inclinations (up to 70°) do not result in a cost function increase larger than 25% and would help reduce noise in latitudes between 60° and 70°. Besides, compared to the ESA Science Study, there exist differences in the orbit selection. While P1 orbit height agrees with a $N_r/N_d = 76/5$ repeating orbit, P2 altitude chosen by Pail et al. (2023) is closer to the $N_r/N_d = 77/5$ resonance. Due to the lower attenuation factor, the weight of P1 in the solution increases. As a consequence, the optimal solution shifts to higher inclinations. This behaviour is illustrated in Fig. 15 (black dashed), artificially adjusting the orbital radius accordingly to Pail et al. (2023). The suggested altitudes however result in a differential drift rate that compromises an optimal overlapping of the ground-tracks.

Global SH synthesis of the global optimal solution is shown in Fig. 16. The optimal solution finds a trade-off between noise at equatorial regions and noise at latitudes above P2 inclination, with latitudes right above P2 inclination subjected to the largest errors. This can be explained because the ground-track is less dense in these areas, only covered by P1, that also suffers from larger altitude attenuation. Furthermore, this region presents the least cross-track sensitivity. Another interesting result is that MAGIC gravity field solutions exhibit inhomogeneous noise in longitude, with a ground-track-related pattern in the projected noise. This aspect has only been observed in operational solutions during resonant months such as September 2004 (see Section 4.1.2). The analytical methodology requires the repeating ground-track constraint to obtain this result.

To assess the expected temporal and spatial resolution of this constellation, commission error is compared to the power of relevant geophysical signals on Earth. For this work, the AOD1B model is employed (Shihora et al., 2022). It accounts for the non-tidal atmosphere and ocean signal, which represent the largest global component of the non-tidal signal variations in sub-weekly temporal scales. Furthermore, we employ the LSDM model (Dill, 2008) to study the hydrology signal. Since the largest variations in hydrology occur beyond the observation period of MAGIC, in monthly timescales, we consider the full signal power to assess the spatial resolution with which it can be observed. Fig. 17 compares the RMS degree spectra in terms of geoid heights for the results of the analytical optimal MAGIC constellation (light blue), geophysical signals, and full end-to-end simulation studies, conveniently adapated from EWH and degree amplitudes if necessary.

Attending to Fig. 17, the optimal MAGIC solution would be able to retrieve the non-tidal atmosphere and ocean variable signal (black) with a spatial resolution of around 300 km, and the hydrology signal below 250 km. The degree spectrum is very similar to an instrument/product-only (PO) simulation provided in ESA Science Study (Pail et al., 2023) (red dashed). When reproducing the scenario with the same design variables and artificially modifying the altitude of the second pair (light blue dashed), there is a good agreement. While these results are expected to fulfil MAGIC mission requirements (Daras et al., 2023a), they are however too optimistic. When compared to full-noise (FN) simulations that incorporate temporal aliasing effects (Bender et al., 2025; Pail et al., 2023), the degree spectra degrades between one or two orders of magnitude. The utility of the analytical methodology must however not be disregarded. For example, if a large constellation was able to observe the undersampled signals that alias at lower timescales, temporal aliasing errors would be significantly mitigated (Gunter et al., 2011; Pfaffenzeller and Pail, 2023; Liu et al., 2024; Zingerle et al., 2024). Thus, the analytical methodology provides an efficient tool to define a lower bound on the attainable improvement.

4.3. Multiple pair missions

Multiple pair constellations have become increasingly interesting in recent years as a promising mission concept for daily and sub-daily gravity field recovery (e.g., Purkhauser and Pail, 2020; Pfaffenzeller and Pail, 2023; Zingerle et al., 2024; Kusche et al., 2025). Additional satellite pairs allow for a denser combined ground-track or sampling a repeating ground-track faster, thus improving spatial or temporal resolution, respectively (Reubelt et al., 2010). Most importantly, since they directly observe the daily and sub-daily non-tidal signals, they can help mitigate temporal aliasing in other GRMs (Gunter et al., 2011). For example, MAGIC would benefit from a multiple pair mission (Kusche et al., 2025). For the same reason,

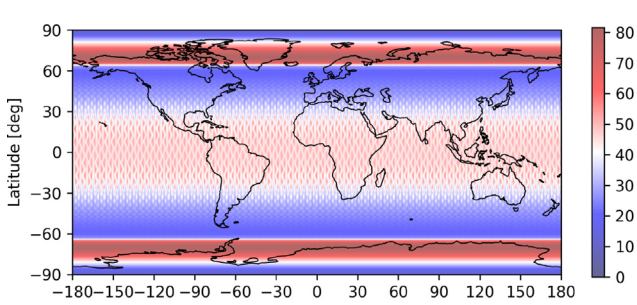

Fig. 16. MAGIC optimal solution EWH synthesis.

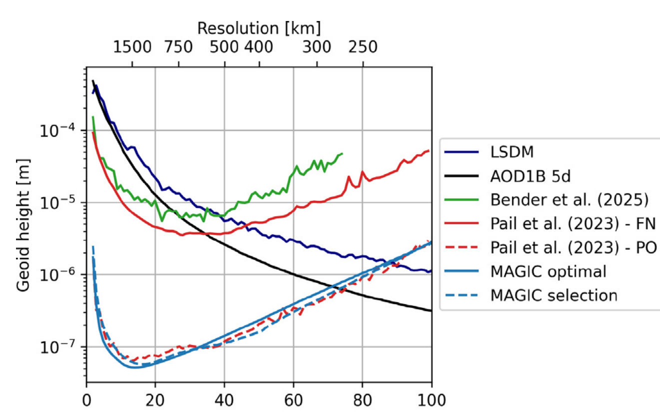

Fig. 17. MAGIC mission RMS degree analysis.

a solution based only on a multiple pair mission is also less affected by temporal aliasing, compared to MAGIC- or GRACE-only solutions (Pfaffenzeller and Pail, 2023).

A multiple pair mission could be conducted with CubeSats to maintain costs affordable. A miniaturized KBR ranging instrument with the same performance as GRACE is realizable in the near future (Pfaffenzeller and Pail, 2023). Moreover, ONERA is currently developing CubeSTAR (Boulanger et al., 2025), a miniaturized accelerometer for CubeSats that is a suitable candidate for multiple pair GRMs. Its approximate performance is considered for this section as:

$$A_{\ddot{r}}(f) = 0.01 \cdot \sqrt{\left(\frac{0.1}{f}\right) + 1 + \left(\frac{f}{0.15}\right)} \, \frac{\mathrm{nm}}{\mathrm{s}^2\sqrt{\mathrm{Hz}}} \tag{40}$$

The performance of multiple pair constellations for daily and sub-daily gravity field recovery is analysed. For this purpose, the inclinations of the off-polar orbital planes are optimized conveniently applying the self-adaptive Differential Evolution algorithm (Brest et al., 2006; Elsayed et al., 2011) with default settings from ESA's PyGMO library (Biscani and Izzo, 2020). The optimization problem is defined as:

$$\begin{aligned} \min_{\mathbf{x}} \quad & f(\mathbf{x}) = \hat{\sigma}_H(\mathbf{x}) \\ \text{s.t.} \quad & x_i - x_{i-1} \leqslant 0, \quad i = 1, \dots, n-1, \\ & x_0 = \pi/2 \end{aligned} \tag{41}$$

with $\mathbf{x} = I_0, I_1, I_2, \dots$ the design variables, i.e. the inclinations of the different orbits. The nominal separation is not co-optimized and set to $\rho_0 = 220\,\mathrm{km}$, following choices for previous and upcoming GRMs. Thus, the full design space is a hypercube with dimension $n-1$, the number of planes to be optimised, since one pair is fixed to a polar orbit $I_0 = 90^\circ$ for global coverage. The full design space is highly multimodal (see Fig. 18), mainly because of nearly-symmetric solutions. Therefore, an inequality constraint is considered as an ordering constraint in Eq. (41), limiting the search space to an $(n-1)$-simplex, which reduces its size by a factor $(n-1)!$ and mitigates multimodality.

Moreover, a cut-off degree of $L = 60$ is chosen, attending to the maximum resolved degrees compared to the non-tidal variable signal (see Fig. 22). The population size is set to $40n$, with n the number of design variables, to promote an expansive exploration of the search space. The evolution is terminated after 20 generations without an improvement of more than 0.1%. For a computer with an estimated floating-point performance of 30 GFLOPs, the cost function is evaluated in 0.1–0.5 s, depending on the sparsity of the normal equations.

Fig. 19 shows the design space of repeating ground-tracks in LEO. Three repeating orbits are selected for study: $N_\mathrm{r}/N_\mathrm{d} = 15/1$, $N_\mathrm{r}/N_\mathrm{d} = 31/2$, $N_\mathrm{r}/N_\mathrm{d} = 46/3$, shown in green. Among the fast repeating orbits, they represent a reasonable trade-off between lower orbits with less attenuation at higher degrees, and higher orbits that allow for longer mission lifetime and are less demanding in terms of propulsion system requirements or accelerometer dynamic range.

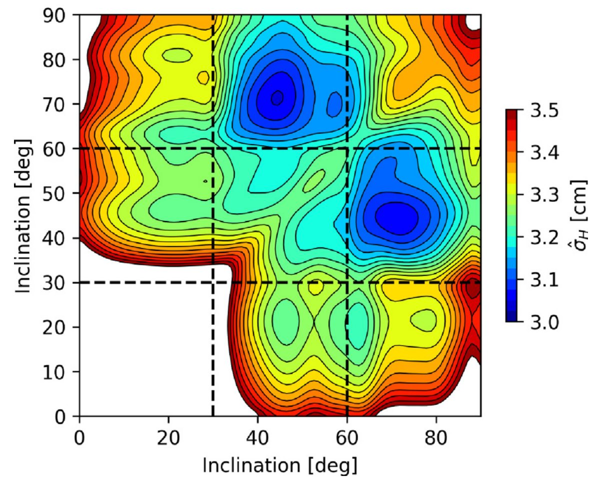

Fig. 18. Multiple pair constellation with $N_\mathrm{r}/N_\mathrm{d} = 15/1$ and 5 different planes: 2D slice of the full design space of inclinations. Three planes are fixed to equispaced inclinations: $30^\circ, 60^\circ, 90^\circ$ (dashed lines). A cut-off degree of $L = 30$ is employed for simplicity.

Fig. 20 shows the optimal inclinations for the different orbits and the number of different ground-tracks. The optimizer finds solutions spreading out the inclinations across the design space. We also compare the optimization results to a latitude-homogeneous inclination policy as suggested by Zingerle et al. (2024), and find improvements ranging from 15% down to less than 5% for more than eight different inclinations, decreasing with increasing number of inclinations (not shown).

Similarly to MAGIC mission (see Fig. 16), synthesis into EWH reveals the imprint of satellite ground-tracks. An example is shown in Fig. 21 for an optimal constellation with a $N_\mathrm{r}/N_\mathrm{d} = 15/1$ repeating ground-track with four different inclinations.

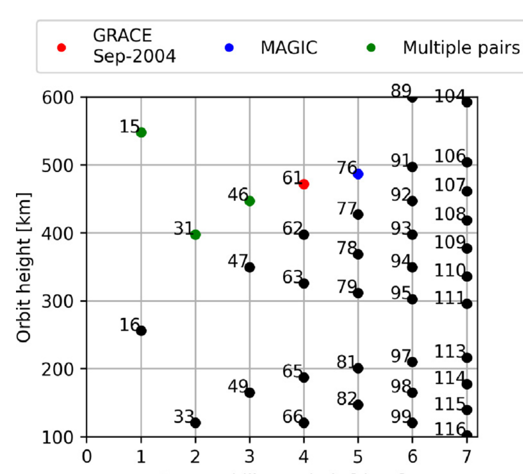

Fig. 19. Repeating ground-tracks in LEO: $I = 90^\circ$.

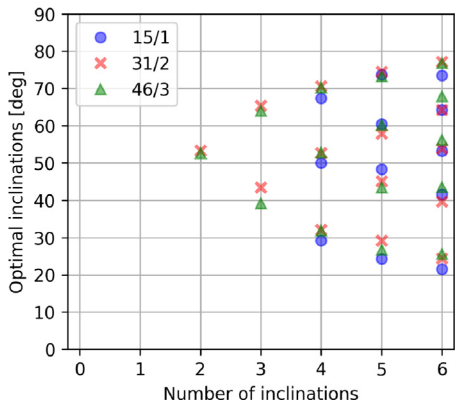

Fig. 20. Multiple pair constellations optimal inclinations.

The RMS degree spectra of optimal solutions for a number of pairs of 6 and 12 is compared to the daily non-tidal atmospheric and ocean signal variation in Fig. 22. The orbital altitude is the main driver when comparing the error of the different repeating orbits, e.g., the $N_r/N_d = 31/2$ orbit has the lowest error because it has a lower orbit height (see also Fig. 19). The intersection with the daily AOD1B signal defines the maximum degree with a signal to noise ratio larger than one. Thus, for example, the $N_r/N_d = 15/1$ orbit resolves up to degree 36 and 40, i.e., a spatial resolution around 550 and 500 km, for 6 and 12 pairs respectively.

The same analysis is extended to any number of pairs up to 12 pairs and any temporal resolution from 6 hours up to 5 days, which represents the full space of undersampled timescales from MAGIC. The results are shown in Fig. 23.

We first discuss the orbit with $N_r/N_d = 15/1$ (Fig. 23a). Above daily timescales, the gains in spatial resolution occur mainly when increasing the number of pairs up to 5. Beyond, the ground-track is already sufficiently dense, additional pairs do not add more information and the improvement stems from observing the same signal with additional observers. A mission with this fast repeating orbit is interesting for sub-daily timescales, allowing for resolution of part of the 6-hourly variable non-tidal signal, up to degree 8 and 18, for 4 and 8 pairs respectively. While the associated temporal resolutions only enable large-scale monitoring, their main contribution would be in de-aliasing for longer timescale missions, e.g., MAGIC.

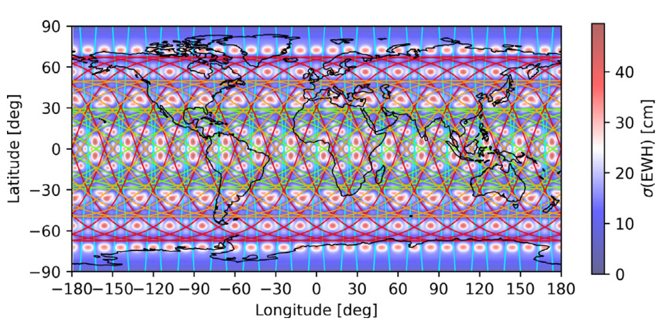

Fig. 21. EWH synthesis of optimal multiple pair constellation $N_r/N_d/N_i = 15/1/4$. Daily gravity field solution.

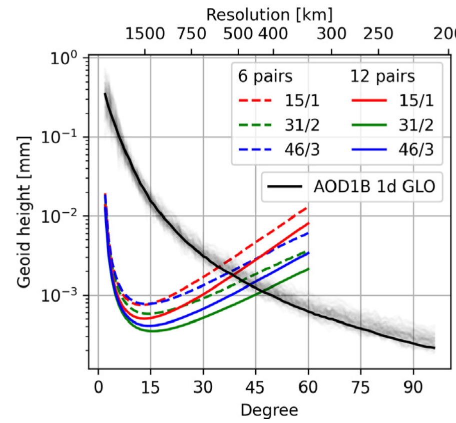

Fig. 22. RMS degree. Multiple pair constellations and AOD1B signal. Daily gravity field solutions.

The two other repeating orbits benefit from a lower altitude showing better spatial resolution above timescales beyond their repeatability period. However, their longer repeatability period compromises the resolution of daily and sub-daily signals, which are meaningful. This can only be circumvented adding sufficiently more pairs. The $N_r/N_d = 46/3$ orbit only outperforms the others in very specific cases for double-pair missions at timescales around 3–4 days, which are not of great interest (e.g., because of MAGIC). Considering also its poor performance at low temporal resolutions, it is not recommend for the range of pairs considered in Fig. 23, but it must not be disregarded as a trade-off solution for larger multiple pair constellations (see Fig. 24). The $N_r/N_d = 31/2$ orbit can be a suitable candidate for a 4-pair mission with 12-hourly temporal resolution that also captures the long-term signal with higher spatial resolution. Furthermore, this orbit achieves the better spatial resolution for the daily signal for a 4-pair mission. Nevertheless, it poses major challenges for the mission, mainly the lower altitude that would compromise mission lifetime, considering the higher area-to-mass ratio of smaller satellites, compared to NGGM, for example.

In Fig. 24, we extrapolate the spatial resolution for the 6-hourly and daily non-tidal atmospheric and ocean signal up to 100 pairs. It can be observed that beyond 8 and 20 pairs for daily and 6-hourly timescales, respectively, the fastest repeating orbit loses its advantage and the performance is mainly driven solely by the orbit altitude.

In summary, the $N_r/N_d = 15/1$ orbit seems to be the appropriate choice for small to medium size multiple pair constellations (below 20 satellite pairs) because of the better observability of temporal signals down to 6-hourly timescales, and the higher altitude, beneficial for mission lifetime or constellation station-keeping. For larger constellation sizes, the performance is driven solely by the orbit altitude. However, proper orbit selection, as is the case for the number of pairs, requires the definition of spatio-temporal requirements to circumvent the temporal aliasing problem.

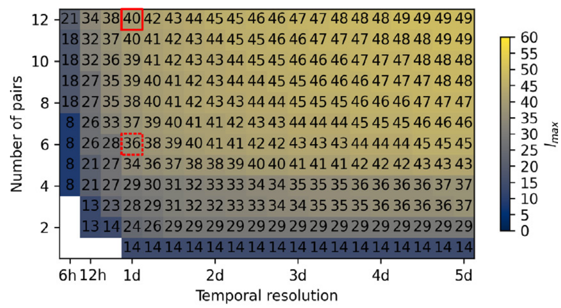

(a) $N_r/N_d = 15/1$

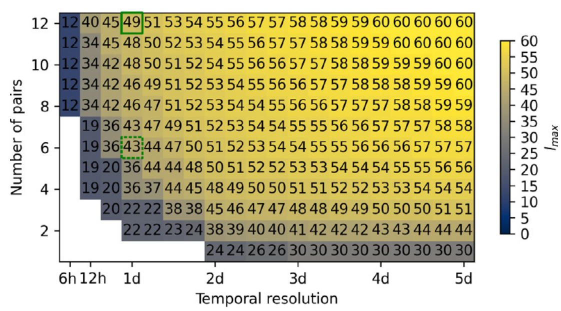

(b) $N_r/N_d = 31/2$

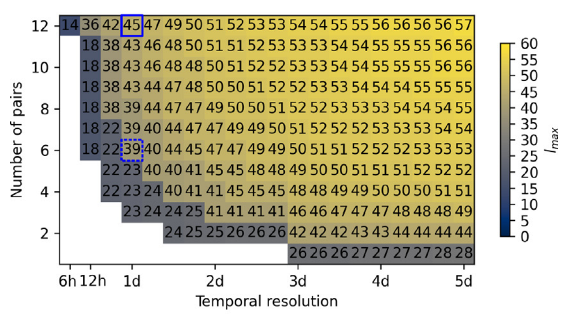

(c) $N_r/N_d = 46/3$

Fig. 23. Optimal multiple pair constellations. Spatio-temporal resolution analysis for the variations in the non-tidal atmospheric and ocean signal. The intersection between the temporal signal power and the error power is shown. The cases from Fig. 22 are highlighted accordingly.

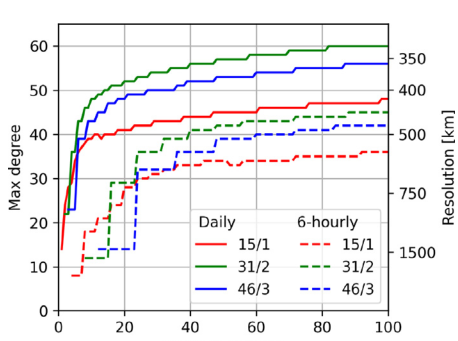

Fig. 24. Multiple pair constellations. Spatial resolution analysis for the 6-hourly and daily variations in the non-tidal atmospheric and ocean signal.

5. Conclusions

This work examined multiple pair constellations for GRMs by means of an analytical error propagation approach based on the lumped coefficients theory. For this purpose, we also incorporated the repeating ground-track constraint to the lumped coefficients.

First, the analytical methodology was validated against GRACE/GRACE-FO operational performance. The analytical methodology underestimated the operational results from ITSG solutions by less than one order of magnitude. However, this was associated with degraded performance of the accelerometers and temporal aliasing effects. Furthermore, we demonstrate that the analytical methodology, through the repeating ground-track constraint, explains the stripes observed operationally in the commission error of ITSG solutions for September 2004. This finding is crucial to properly model multiple pair missions that leverage resonant orbits.

MAGIC mission was simulated for one of the potential repeating ground-tracks. The nominal inter-satellite distance and the inclination of the second-pair were co-optimized, finding a global optimum through the exploration of the whole design space. This allowed for identifying crucial properties of the optimization landscape, namely a shallow global minimum and the common attenuation modes. The global optimal found ($\rho_0 = 297$ km, $I_2 = 61.5^\circ$) differs from selections from full end-to-end simulation-based studies (e.g., ESA/NGGM Science Study $\rho_0 = 220$ km, $I_2 = 70^\circ$). Nonetheless, nearly-optimal solutions might benefit other mission aspects, such as a formation stability or better observation of higher latitudes. Moreover, the inhomogeneous error pattern of MAGIC gravity field solutions was demonstrated, with largest errors identified for latitudes right above the inclination of the second pair. Comparison of the degree spectra shows good agreement between the analytical methodology and an instrument-only full end-to-end simulation from ESA/NGGM Science Study. For this solution, the observability of the atmospheric and ocean non-tidal signal was analysed through the AOD1B product. It was concluded that the optimized constellation would resolve the variable atmospheric and ocean non-tidal signal up to roughly 300 km, for a temporal resolution of five days. We also analyse the resolution of the hydrology signal through the LSDM model, obtaining an attainable resolution of 250 km. These results would enable resolving key catchment basins currently at the limit of satellite gravimetry resolution, for example (Pail et al., 2015). Moreover, it would allow for better observation of sub-weekly geophysical processes such as mesoscale solid Earth and ocean tides, ocean bottom pressure signal, slow earthquakes or atmosphere dynamics, among others (Sneeuw et al., 2004). Lastly, it would lead to less reliance on de-aliasing models and better signal separation (Pail et al., 2015). Nonetheless, end-to-end simulation studies show that the effect of temporal aliasing degrades the actual performance more than one order of magnitude (e.g., Pail et al., 2023). For this reason, we explore multiple pair missions to observe the undersampled daily and sub-daily signals.

Multiple pair constellations for daily and sub-daily gravity field recovery were optimized for cost-effective performance based on miniaturized instruments. Thus, CubeSat-based multiple pair missions were simulated for up to twelve satellite pairs for three different orbits from the space of fast-repeating orbits in LEO. The performance of each mission was defined relative to the maximum observable degree of the variable non-tidal atmospheric and ocean signal, characterising the temporal resolution for timescales from 6 hours up to 5 days. Besides, the spatial resolution for the 6-hourly and daily signals was studied up to 100 pairs. The $N_\mathrm{r}/N_\mathrm{d} = 15/1$ orbit provides the best observability of the 6-hourly signal for small to medium size constellations (up to 20 pairs). Furthermore, given its higher altitude, it benefits mission lifetime. For any number of pairs, the $N_\mathrm{r}/N_\mathrm{d} = 31/2$ orbit dominates above daily timescales, because of the lower orbit altitude. For semi-diurnal or diurnal signals, the former repeating orbit is preferable for a low number of pairs, while the latter dominates for larger constellations, since the spatial resolution of larger constellations is solely driven by orbit height. The selection of an optimal repeating orbit and the definition of an appropriate number of pairs are not trivial. For this purpose, requirements for the spatial resolution for every timescale must be defined, thereby enabling the de-aliasing of longer timescale missions.

While the analytical methodology employed in this study allows for very efficient simulation of GRMs performance, it has limitations that must be carefully considered. The diagonal observation covariance requires the stationarity of the error sources. Furthermore, the necessary periodicity condition constrains the scenarios to be analysed. For example, application to missions with ground-tracks with different repeatability periods or partial ground-track coverage is either complex or not possible. Lastly, the main limitation is associated with background error models. They are known to degrade the quality of the gravity field solutions, but have not been considered.

Code availability

The software library GFEAT has been employed for this work and the source code is available in https://github.com/gabri-aero/gfeat.

Declaration of competing interest

The authors declare that they have no known competing financial interests or personal relationships that could have appeared to influence the work reported in this paper.

Acknowledgments

The authors acknowledge the open access funding provided by Graz University of Technology. We also thank Torsten Mayer-Gürr for the discussions on the operational data processing for the ITSG gravity field solutions.

References

Abich, K., Abramovici, A., Amparan, B., Baatzsch, A., Okihiro, B.B., Barr, D.C., Bize, M.P., Bogan, C., Braxmaier, C., Burke, M.J., Clark, K.C., Dahl, C., Dahl, K., Danzmann, K., Davis, M.A., de Vine, G., Dickson, J.A., Dubovitsky, S., Eckardt, A., Ester, T., Barranco, G.F., Flatscher, R., Flechtner, F., Folkner, W.M., Francis, S., Gilbert, M.S., Gilles, F., Gohlke, M., Grossard, N., Guenther, B., Hager, P., Hauden, J., Heine, F., Heinzel, G., Herding, M., Hinz, M., Howell, J., Katsumura, M., Kaufer, M., Klipstein, W., Koch, A., Kruger, M., Larsen, K., Lebeda, A., Lebeda, A., Leikert, T., Liebe, C.C., Liu, J., Lobmeyer, L., Mahrdt, C., Mangoldt, T., McKenzie, K., Misfeldt, M., Morton, P.R., Müller, V., Murray, A.T., Nguyen, D.J., Nicklaus, K., Pierce, R., Ravich, J.A., Reavis, G., Reiche, J., Sanjuan, J., Schütze, D., Seiter, C., Shaddock, D., Sheard, B., Sileo, M., Spero, R., Spiers, G., Stede, G., Stephens, M., Sutton, A., Trinh, J., Voss, K., Wang, D., Wang, R.T., Ware, B., Wegener, H., Windisch, S., Woodruff, C., Zender, B., Zimmermann, M., 2019. In-orbit performance of the GRACE follow-on laser ranging interferometer. Phys. Rev. Lett. 123, 031101. https://doi.org/10.1103/physrevlett.123.031101.

Airbus Defence and Space, 2022. Astrix® 120 — Very High Performance FOG Fibre Optic Inertial Measurement Unit for Space Multi-Application (v3). Technical Datasheet, Airbus Defence and Space. URL: https://www.airbus.com/sites/g/files/jlcbta136/files/2022-02/ScE-AVIONICS-ASTRIX120v3_2022.pdf.

Baldesarra, M., Brieden, P., Danzmann, K., Daras, B., Doll, B., Feili, D., Flechtner, F., Flury, J., Gruber, T., Heinzel, G., Iran Pour, S., Kusche, J., Langemann, M., Lücher, A., Müller, J., Müller, V., Murböck, M., Naeimi, M., Pail, R., Raimondo, J.C., Reiche, J., Reubelt, T., Sheard, B., Sneeuw, N., 2014. e2.motion - Earth System Mass Transport Mission (Square) - Concept for a Next Generation Gravity Field Mission - Final Report of Project "Satellite Gravimetry of the Next Generation (NGGM-D)". Technical Report 318. Deutsche Geodätische Kommission der Bayerischen Akademie der Wissenschaften. Munich, Germany. Final report of project NGGM-D, NGGM-D Team.

Balmino, G., Schrama, E., Sneeuw, N., 1996. Compatibility of first-order circular orbit perturbations theories; consequences for cross-track inclination functions. J. Geodesy 70, 554–561. https://doi.org/10.1007/bf00867863.

Bandikova, T., 2015. The role of attitude determination for inter-satellite ranging Ph.D. thesis. Leibniz Universität Hannover. Deutsche Geodätische Kommission.

Bender, P.L., Conklin, J.W., Wiese, D.N., 2025. Short-period mass variations and the next generation gravity mission. J. Geophys. Res.: Solid Earth 130. https://doi.org/10.1029/2024jb030290.

Bender, P.L., Wiese, D.N., Nerem, R.S., 2008. A possible dual-GRACE mission with 90 degree and 63 degree inclination orbits, in: Missions, Technologies (Eds.), Proceedings of the Third International Symposium on Formation Flying, pp. 1–6.

Biscani, F., Izzo, D., 2020. A parallel global multiobjective framework for optimization: pagmo. Journal of Open Source Software 5, 2338. URL: https://doi.org/10.21105/joss.02338, doi:10.21105/joss.02338.

Boulanger, D., Christophe, B., Lebat, V., Liorzou, F., Maquaire, K., Portier, N., Rodrigues, M., 2025. CubeSTAR: a tiny space accelerometer for Earth observation applications. In: Petrozzi-Ilstad, M. (Ed.), Small Satellites Systems and Services Symposium (4S 2024), SPIE. p. 87. doi:10.1117/12.3062066.

Brest, J., Greiner, S., Boskovic, B., Mernik, M., Zumer, V., 2006. Self-adapting control parameters in differential evolution: a comparative study on numerical benchmark problems. IEEE Trans. Evol. Comput. 10, 646–657. https://doi.org/10.1109/tevc.2006.872133.

Brouwer, D., 1959. Solution of the problem of artificial satellite theory without drag. Astron. J. 64, 378. https://doi.org/10.1086/107958.

Cesare, S., Dionisio, S., Saponara, M., Bravo-Berguño, D., Massotti, L., Teixeira da Encarnação, J., Christophe, B., 2022. Drag and attitude control for the Next Generation Gravity Mission. Remote Sens. 14, 2916. https://doi.org/10.3390/rs14122916.

Christophe, B., Boulanger, D., Foulon, B., Huynh, P.A., Lebat, V., Liorzou, F., Perrot, E., 2015. A new generation of ultra-sensitive electrostatic accelerometers for GRACE Follow-on and towards the next generation gravity missions. Acta Astronaut. 117, 1–7. https://doi.org/10.1016/j.actaastro.2015.06.021.

Christophe, B., Foulon, B., Liorzou, F., Lebat, V., Boulanger, D., Huynh, P.A., Zahzam, N., Bidel, Y., Bresson, A., 2018. Status of development of the future accelerometers for next generation gravity missions. In: International Symposium on Advancing Geodesy in a Changing World. Springer International Publishing, pp. 85–89. https://doi.org/10.1007/1345_2018_42.

Colombo, O.L., 1984. The global mapping of gravity with two satellites. Rijkscommissie voor Geodesie.

Daras, I., March, G., Mass Chnge Mission Expert Group, J., Wiese, D., Blackwood, C., Forman, F., Loomis, B., Luthcke, S., Peralta-Ferriz, C., Sauber-Rosenberg, J., Eicker, A., Panet, I., Visser, P., Meyssignac, B., Wouters, B., Bamber, J., Pail, R., Flechtner, F., 2023a. Next generation gravity mission (NGGM) mission requirements document. doi:10.5270/esa.nggm-mrd.2023-09-v1.0.

Daras, I., March, G., Pail, R., Hughes, C.W., Braitenberg, C., Güntner, A., Eicker, A., Wouters, B., Heller-Kaikov, B., Pivetta, T., Pastorutti, A., 2023b. Mass-change And Geosciences International Constellation (MAGIC) expected impact on science and applications. Geophys. J. Int. 236, 1288–1308. https://doi.org/10.1093/gji/ggad472.

Daras, I., Pail, R., 2017. Treatment of temporal aliasing effects in the context of next generation satellite gravimetry missions. J. Geophys. Res.: Solid Earth 122, 7343–7362. https://doi.org/10.1002/2017jb014250.

Dill, R., 2008. Hydrological model LSDM for operational Earth rotation and gravity field variations. Scientific Technical Report STR 08/09. https://doi.org/10.2312/GFZ.B103-08095.

Drinkwater, M.R., Haagmans, R., Muzi, D., Popescu, A., Floberghagen, R., Kern, M., Fehringer, M., 2007. The GOCE Gravity Mission: ESA's First Core Earth Explorer. In: Proceedings of 3rd International GOCE User Workshop, ESA, Frascati, Italy, pp. 1–8.

Ellmer, M., 2011. Optimization of the orbit parameters of future gravity missions using genetic algorithms. https://doi.org/10.18419/OPUS-3873.

Ellmer, M., 2018. Contributions to GRACE gravity field recovery Ph.D. thesis. Technische Universität Graz. https://doi.org/10.3217/N000G-EFZ85.

Elsaka, B., 2014. Feasible multiple satellite mission scenarios flying in a constellation for refinement of the gravity field recovery. Int. J. Geosci. 05, 267–273. https://doi.org/10.4236/ijg.2014.53027.

Elsayed, S.M., Sarker, R.A., Essam, D.L., 2011. Differential evolution with multiple strategies for solving CEC2011 real-world numerical optimization problems. In: 2011 IEEE Congress of Evolutionary Computation (CEC), IEEE, pp. 1041–1048. https://doi.org/10.1109/cec.2011.5949732.

Teixeira da Encarnação, J., Arnold, D., Bezdek, A., Dahle, C., Doornbos, E., van den IJssel, J., Jäggi, A., Mayer-Gürr, T., Sebera, J., Visser, P., Zehentner, N., 2016. Gravity field models derived from Swarm GPS data. Earth, Planets and Space 68. doi:10.1186/s40623-016-0499-9.

Encarnação, J., Siemes, C., Daras, I., Carraz, O., Strangfeld, A., Zingerle, P., Pail, R., 2026. A path towards effective exploitation of quantum sensors in future satellite gravity missions. Adv. Space Res. 77, 4121–4151. https://doi.org/10.1016/j.asr.2025.12.053.

Famiglietti, J.S., Rodell, M., 2013. Water in the balance. Science 340, 1300–1301. https://doi.org/10.1126/science.1236460.

Flechtner, F., Neumayer, K.H., Dahle, C., Dobslaw, H., Fagiolini, E., Raimondo, J.C., Güntner, A., 2015. What can be expected from the GRACE-FO laser ranging interferometer for earth science applications? Surv. Geophys. 37, 453–470. https://doi.org/10.1007/s10712-015-9338-y.

Goossens, S., Sabaka, T.J., Wieczorek, M.A., Neumann, G.A., Mazarico, E., Lemoine, F.G., Nicholas, J.B., Smith, D.E., Zuber, M.T., 2020. High-resolution gravity field models from GRAIL data and implications for models of the density structure of the moon's crust. J. Geophys. Res.: Planets 125. https://doi.org/10.1029/2019je006086.

Goswami, S., Francis, S.P., Bandikova, T., Spero, R.E., 2021. Analysis of GRACE follow-on laser ranging interferometer derived inter-satellite pointing angles. IEEE Sens. J. 21, 19209–19221. https://doi.org/10.1109/jsen.2021.3090790.

Gunter, B.C., Encarnacao, J., Ditmar, P., Klees, R., 2011. Using satellite constellations for improved determination of earth's time-variable gravity. J. Spacecr. Rock. 48, 368–377. https://doi.org/10.2514/1.50926.

Guo, D.H., Wang, C.Q., Zhu, Z.T., et al., 2024. A simulation study on uncertainties and spatio-temporal resolutions of time-variable gravity fields based on multiple GRACE-like constellations. Chinese J. Geophys. (in Chinese) 67, 2125–2140. https://doi.org/10.6038/cjg2023R0422.

Haagmans, R., Tsaoussi, L., Masotti, L., March, G., Daras, I., 2020. Next generation gravity mission as a mass-change and geosciences international constellation (MAGIC) - A joint ESA/NASA double-pair mission based on NASA's MCDO and ESA's NGGM studies. Technical Report. ESA. URL: https://esamultimedia.esa.int/docs/EarthObservation/MAGIC_NGGM_MCDO_MRD_v1_0-signed2.pdf.

Haagmans, R., van Gelderen, M., 1991. Error variances-covariances of GEM-T1: their characteristics and implications in geoid computation. J. Geophys. Res.: Solid Earth 96, 20011–20022. https://doi.org/10.1029/91jb01971.

Han, S., Jekeli, C., Shum, C.K., 2004. Time-variable aliasing effects of ocean tides, atmosphere, and continental water mass on monthly mean GRACE gravity field. J. Geophys. Res.: Solid Earth 109. https://doi.org/10.1029/2003jb002501.

Heiskanen, W., Moritz, H., 1967. Physical Geodesy. Series of books in geology, W.H. Freeman.

Hill, G.W., 1878. Researches in the lunar theory. Am. J. Math. 1, 5. https://doi.org/10.2307/2369430.

Hladczuk, N., van den IJssel, J., Jacobs, F., Siemes, C., Visser, P., 2025. Solar and thermal radiation pressure modelling for improving the GOCE horizontal wind dataset. Advances in Space Research 76, 6899–6917. doi:10.1016/j.asr.2025.09.043.

Iran Pour, S., Sneeuw, N., Weigelt, M., Amiri-Simkooei, A., 2019. Orbit optimization for future satellite gravity field missions: influence of the time variable gravity field models in a genetic algorithm approach. In: IX Hotine-Marussi Symposium on Mathematical Geodesy, Springer International Publishing. pp. 3–9. doi:10.1007/1345_2019_79.

Jacobs, F., Hladczuk, N., van den IJssel, J., Siemes, C., Visser, P., 2026. Joint optimization of a GRACE radiation pressure model, the accelerometer scale factors, and an empirical magnetic-field-induced accelerometer bias. Adv. Space Res., 77, 12096–12121. doi:10.1016/j.asr.2026.04.043.

Jäggi, A., Prange, L., Hugentobler, U., 2011. Impact of covariance information of kinematic positions on orbit reconstruction and gravity field recovery. Adv. Space Res. 47, 1472–1479. https://doi.org/10.1016/j.asr.2010.12.009.

Kaula, W.M., 1959. Statistical and harmonic analysis of gravity. J. Geophys. Res. 64, 2401–2421. https://doi.org/10.1029/jz064i012p02401.

Kaula, W.M., 1966. Theory of Satellite Geodesy: Applications of Satellites to Geodesy. Blaisdell Publishing Company.

Kim, J., Tapley, B.D., 2002. Error analysis of a low-low satellite-to-satellite tracking mission. J. Guid., Control, Dynam. 25, 1100–1106. https://doi.org/10.2514/2.4989.

Klinger, B., 2018. A contribution to GRACE time-variable gravity field recovery Ph.D. thesis. Technische Universität Graz. https://doi.org/10.3217/4NWH1-24657.

Klokocník, J., Wagner, C.A., Kostelecký, J., Bezdek, A., Novák, P., McAdoo, D., 2008. Variations in the accuracy of gravity recovery due to ground track variability: GRACE, CHAMP, and GOCE. J. Geodesy 82, 917–927. https://doi.org/10.1007/s00190-008-0222-0.

Knudsen, P., Andersen, O., 2002. Correcting GRACE gravity fields for ocean tide effects. Geophys. Res. Lett. 29. https://doi.org/10.1029/2001gl014005.

Koop, R., 1993. Global gravity field modelling using satellite gravity gradiometry. Rijkscommissie voor Geodesie.

Kornfeld, R.P., Arnold, B.W., Gross, M.A., Dahya, N.T., Klipstein, W. M., Gath, P.F., Bettadpur, S., 2019. GRACE-FO: the gravity recovery and climate experiment follow-on mission. J. Spacecr. Rock. 56, 931–951. https://doi.org/10.2514/1.a34326.

Kusche, J., Strohmenger, C., Gerdener, H., Uebbing, B., Springer, A., Ewerdwalbesloh, Y., Eicker, A., Braitenberg, C., Pastorutti, A., Pail, R., Zingerle, P., Schlaak, M., Reguzzoni, M., Rossi, L., Migliaccio, F., Daras, I., 2025. Benefit of MAGIC and multipair quantum satellite gravity missions in Earth science applications. Geophys. J. Int. 242. https://doi.org/10.1093/gji/ggaf195.

Kvas, A., Behzadpour, S., Ellmer, M., Klinger, B., Strasser, S., Zehentner, N., Mayer-Gürr, T., 2019. ITSG-Grace2018: overview and evaluation of a new GRACE-only gravity field time series. J. Geophys. Res.: Solid Earth 124, 9332–9344. https://doi.org/10.1029/2019jb017415.

Kvas, A., Mayer-Gürr, T., 2019. GRACE gravity field recovery with background model uncertainties. J. Geodesy 93, 2543–2552. https://doi.org/10.1007/s00190-019-01314-1.

Landerer, F.W., Flechtner, F.M., Save, H., Webb, F.H., Bandikova, T., Bertiger, W.I., Bettadpur, S.V., Byun, S.H., Dahle, C., Dobslaw, H., Fahnestock, E., Harvey, N., Kang, Z., Kruizinga, G.L.H., Loomis, B. D., McCullough, C., Murböck, M., Nagel, P., Paik, M., Pie, N., Poole, S., Strekalov, D., Tamisiea, M.E., Wang, F., Watkins, M.M., Wen, H., Wiese, D.N., Yuan, D., 2020. Extending the global mass change data record: GRACE follow-on instrument and science data performance. Geophys. Res. Lett. 47. https://doi.org/10.1029/2020gl088306.

Li, H., Reubelt, T., Antoni, M., Sneeuw, N., 2016. Gravity field error analysis for pendulum formations by a semi-analytical approach. J. Geodesy 91, 233–251. https://doi.org/10.1007/s00190-016-0958-x.

Liu, Y., Li, J., Xu, X., Wei, H., Li, Z., Zhao, Y., 2024. Simulation analysis of recovering time-varying gravity fields based on Starlink-like constellation. Geophys. J. Int. 239, 402–418. https://doi.org/10.1093/gji/ggae273.

Loomis, B.D., Nerem, R.S., Luthcke, S.B., 2011. Simulation study of a follow-on gravity mission to GRACE. J. Geodesy 86, 319–335. https://doi.org/10.1007/s00190-011-0521-8.

Luo, P., Jin, S., Shi, Q., 2022. Undifferenced kinematic precise orbit determination of swarm and GRACE-FO satellites from GNSS Observations. Sensors 22, 1071. https://doi.org/10.3390/s22031071.

Lévèque, T., Fallet, C., Lefebve, J., Piquereau, A., Gauguet, A., Battelier, B., Bouyer, P., Gaaloul, N., Lachmann, M., Piest, B., Rasel, E., Müller, J., Schubert, C., Beaufils, Q., Pereira Dos Santos, F., 2023. CARIOQA: definition of a Quantum Pathfinder Mission, in: Minoglou, K., Karafolas, N., Cugny, B. (Eds.), International Conference on Space Optics — ICSO 2022, SPIE. p. 129. doi:10.1117/12.2690536.

Malossi, N., Bodart, Q., Merlet, S., Lévèque, T., Landragin, A., Santos, F. P.D., 2010. Double diffraction in an atomic gravimeter. Phys. Rev. A 81, 013617. https://doi.org/10.1103/physreva.81.013617.

Massotti, L., Bulit, A., Daras, I., Carnicero Dominguez, B., Carraz, O., Hall, K., Heliere, A., March, G., Marchese, V., Martimort, P., Palmer, K., Rodrigues, G., Silvestrin, P., Wallace, N., 2023. Next Generation Gravity Mission design activities within the MAGIC - MAss Change and Geoscience International - Constellation. https://doi.org/10.5194/egusphere-egu23-14482.

Mayer-Gürr, T., 2006. Gravitationsfeldbestimmung aus der Analyse kurzer Bahnbögen am Beispiel der Satellitenmissionen CHAMP und GRACE Ph.D. thesis. Rheinische Friedrich-Wilhelms-Universität Bonn.

Mayer-Gürr, T., Behzadpur, S., Ellmer, M., Kvas, A., Klinger, B., Strasser, S., Zehentner, N., 2018. ITSG-Grace2018 - Monthly. Daily and Static Gravity Field Solutions from GRACE. https://doi.org/10.5880/ICGEM.2018.003.

Murböck, M., Abrykosov, P., Dahle, C., Hauk, M., Pail, R., Flechtner, F., 2023. In-orbit performance of the GRACE accelerometers and microwave ranging instrument. Remote Sens. 15, 563. https://doi.org/10.3390/rs15030563.

Nicklaus, K., Voss, K., Feiri, A., Kaufer, M., Dahl, C., Herding, M., Curzadd, B.A., Baatzsch, A., Flock, J., Weller, M., Müller, V., Heinzel, G., Misfeldt, M., Delgado, J.J.E., 2022. Towards NGGM: laser tracking instrument for the next generation of gravity missions. Remote Sens. 14, 4089. https://doi.org/10.3390/rs14164089.

Pail, R., Bingham, R., Braitenberg, C., Dobslaw, H., Eicker, A., Güntner, A., Horwath, M., Ivins, E., Longuevergne, L., Panet, I., Wouters, B., Team, t., 2015. Observing mass transport to understand global change and to benefit society: science and user needs: an international multi-disciplinary initiative for IUGG. WorkingPaper 320. Verlag der Bayerischen Akademie der Wissenschaften in Kommission beim Verlag C.H. Beck.

Pail, R., Gruber, T., Abrykosov, P., Zingerle, P., Visser, P., Teixeira da Encarnação, J., Siemes, C., Flechtner, F., Dahle, C., Hauk, M., Wilms, J., Bruinsma, S., Marty, J.C., Müller, V., Müller, L., 2023. Final Report NGGM/MAGIC – Science Support Study During Phase A – CCN1. Technical Report MAGIC-CCN1_FR 1.0. Technische Universität München.

Pail, R., Wermut, M., 2003. GOCE SGG and SST quick-look gravity field analysis. Adv. Geosci. 1, 5–9. https://doi.org/10.5194/adgeo-1-5-2003.

Pfaffenzeller, N., Pail, R., 2023. Small satellite formations and constellations for observing sub-daily mass changes in the Earth system. Geophys. J. Int. 234, 1550–1567. https://doi.org/10.1093/gji/ggad132.

Purkhauser, A.F., Pail, R., 2020. Triple-pair constellation configurations for temporal gravity field retrieval. Remote Sens. 12, 831. https://doi.org/10.3390/rs12050831.

Reigber, C., Balmino, G., Schwintzer, P., Biancale, R., Bode, A., Lemoine, J., König, R., Loyer, S., Neumayer, H., Marty, J., Barthelmes, F., Perosanz, F., Zhu, S.Y., 2002. A high-quality global gravity field model from CHAMP GPS tracking data and accelerometry (EIGEN-1S). Geophys. Res. Lett. 29. https://doi.org/10.1029/2002gl015064.

Reubelt, T., Sneeuw, N., Sharifi, M.A., 2010. Future Mission Design Options for Spatio-Temporal Geopotential Recovery. Springer, Berlin Heidelberg, pp. 163–170. https://doi.org/10.1007/978-3-642-10634-7_22.

Rosborough, G.W., Tapley, B.D., 1987. Radial, transverse and normal satellite position perturbations due to the geopotential. Celest. Mech. 40, 409–421. https://doi.org/10.1007/bf01235855.

Rummel, R., Balmino, G., Johannessen, J., Visser, P., Woodworth, P., 2002. Dedicated gravity field missions—principles and aims. J. Geodyn. 33, 3–20. https://doi.org/10.1016/s0264-3707(01)00050-3.

Rummel, R., Colombo, O.L., 1985. Gravity field determination from satellite gradiometry. Bulletin Géodésique 59, 233–246. https://doi.org/10.1007/bf02520329.

Schrama, E.J.O., 1989. The role of orbit errors in processing of satellite altimeter data. In: Number 33 in Publications on geodesy, Rijkscommissie voor Geodesie, Delft, The Netherlands.

Schrama, E.J.O., 1990. Gravity field error analysis: Applications of GPS receivers and gradiometers on low orbiting platforms. Technical Report. NASA.

Schrama, E.J.O., 1991. Gravity field error analysis: applications of global positioning system receivers and gradiometers on low orbiting platforms. J. Geophys. Res.: Solid Earth 96, 20041–20051. https://doi.org/10.1029/91jb01972.

Sharifi, M., Sneeuw, N., Keller, W., 2007. Gravity recovery capability of four generic satellite formations, in: Proceedings of the Symposium "Gravity Field of the Earth", General Command of Mapping. pp. 211–216.

Shihora, L., Balidakis, K., Dill, R., Dahle, C., Ghobadi-Far, K., Bonin, J., Dobslaw, H., 2022. Non-tidal background modeling for satellite gravimetry based on operational ECWMF and ERA5 Reanalysis Data: AOD1B RL07. J. Geophys. Res.: Solid Earth 127. https://doi.org/10.1029/2022jb024360.

Siemes, C., Borries, C., Bruinsma, S., Fernandez-Gomez, I., Hladczuk, N., den IJssel, J., Kodikara, T., Vielberg, K., Visser, P., 2023. New thermosphere neutral mass density and crosswind datasets from CHAMP, GRACE, and GRACE-FO. Journal of Space Weather and Space Climate 13, 16. doi:10.1051/swsc/2023014.

Sneeuw, N., 2000. A Semi-Analytical Approach to Gravity Field Analysis from Satellite Observations Ph.D. thesis. Institut für Astronomische und Physikalische Geodäsie, TU München.

Sneeuw, N., Flury, J., Rummel, R., 2004. Science requirements on future missions and simulated mission scenarios. Earth, Moon, and Planets 94, 113–142. https://doi.org/10.1007/s11038-004-7605-x.

Tapley, B.D., Bettadpur, S., Watkins, M., Reigber, C., 2004. The gravity recovery and climate experiment: mission overview and early results. Geophys. Res. Lett. 31. https://doi.org/10.1029/2004gl019920.

Valles-Valverde, G., 2025. Analytic error analysis of orbital configurations for gravity research missions Master's thesis. TU Delft.

Visser, P., 2005. Low-low satellite-to-satellite tracking: a comparison between analytical linear orbit perturbation theory and numerical integration. J. Geodesy 79, 160–166. https://doi.org/10.1007/s00190-005-0455-0.

Visser, P.N.A.M., Schrama, E.J.O., Sneeuw, N., Weigelt, M., 2012. Dependency of Resolvable Gravitational Spatial Resolution on Space-Borne Observation Techniques. In: Kenyon, S., Pacino, M.C., Marti, U. (Eds.), Geodesy for Planet Earth. Springer, Berlin Heidelberg, Berlin, Heidelberg, pp. 373–379.

Wagner, C.A., 1983. Direct determination of gravitational harmonics from low-low GRAVSAT data. J. Geophys. Res.: Solid Earth 88, 10309–10321. https://doi.org/10.1029/jb088ib12p10309.

Wahr, J., Molenaar, M., Bryan, F., 1998. Time variability of the Earth's gravity field: Hydrological and oceanic effects and their possible detection using GRACE. J. Geophys. Res.: Solid Earth 103, 30205–30229. https://doi.org/10.1029/98jb02844.

Wiese, D.N., Nerem, R.S., Lemoine, F.G., 2011. Design considerations for a dedicated gravity recovery satellite mission consisting of two pairs of satellites. J. Geodesy 86, 81–98. https://doi.org/10.1007/s00190-011-0493-8.

Wiese, D.N., Visser, P., Nerem, R.S., 2011. Estimating low resolution gravity fields at short time intervals to reduce temporal aliasing errors. Adv. Space Res. 48, 1094–1107. https://doi.org/10.1016/j.asr.2011.05.027.

Wolff, M., 1969. Direct measurements of the Earth's gravitational potential using a satellite pair. J. Geophys. Res. 74, 5295–5300. https://doi.org/10.1029/jb074i022p05295.

Wu, S.C., Kruizinga, G., Bertiger, W., 2006. Algorithm theoretical basis document for GRACE Level-1B data processing V1.2. Technical Report. JPL.

Zingerle, P., Gruber, T., Pail, R., Daras, I., 2024. Constellation design and performance of future quantum satellite gravity missions. Earth, Planets and Space 76. https://doi.org/10.1186/s40623-024-02034-3.

Zuber, M.T., Smith, D.E., Watkins, M.M., Asmar, S.W., Konopliv, A.S., Lemoine, F.G., Melosh, H.J., Neumann, G.A., Phillips, R.J., Solomon, S.C., Wieczorek, M.A., Williams, J.G., Goossens, S.J., Kruizinga, G., Mazarico, E., Park, R.S., Yuan, D.N., 2013. Gravity field of the moon from the gravity recovery and interior laboratory (GRAIL) Mission. Science 339, 668–671. https://doi.org/10.1126/science.1231507.